On the phenomenon of ionic wind induced by corona discharges

Eric Moreau

On the phenomenon of ionic wind induced by corona discharges

Eric MOREAU

University of Poitiers, Pprime institute, CNRS UPR 3346, ISAE-ENSMA

Téléport 2, BP 30179, 86962 Futuroscope, France

corresponding author: eric.moreau@univ-poitiers.fr

Abstract

This article reviews the latest knowledge on ionic wind generated by two-electrode volume corona discharges in atmospheric air. We aim to accurately describe the ionic wind topology and explain its properties based on experimental measurements and numerical simulations. The two geometric configurations most commonly discussed in this article are the point-plate and point-ring. After an introduction and brief theoretical overview of the physical phenomenon, we describe the different regimes of DC and AC corona discharges, as they play a key role in the properties of the induced ionic wind. Then, in the third part, we discuss the time-averaged characteristics of the ionic wind. We show that positive corona discharges produce a sharp, pointed, and fast ionic wind jet, especially when breakdown streamers are present. On the contrary, the negative corona discharges usually produce a wider and slower air jet. In the fourth part, we describe the air movement from the tip when high voltage is switched on. Moreover, we highlight that the Trichel pulses and the breakdown streamers play a fundamental role in the ionic wind dynamics. Finally, in the last part of this article, we focus on numerical simulations of ionic wind to explain all the experimental results presented earlier. Indeed, the origin of the ionic wind is the electrohydrodynamic force produced by the discharge. To determine this force, we need to know the electric field distribution and the

density of electrons and ions everywhere in space at all times, which is achievable only through numerical simulations. To conclude, it can be said that research over the past ten years has led to a much better understanding of the ionic wind phenomenon, particularly regarding the role of unsteady and very fast phenomena such as Trichel pulses and breakdown streamers. However, there is still a lot of experimental and numerical simulation work to be done to optimize all the input parameters of the discharge according to the targeted application. And since the applications of ionic wind will most likely be at small scales, down to the sub-millimeter scale, it will also be necessary to study the behavior of corona discharges and the ionic wind they can generate at this scale.

1. Introduction

When a sufficiently high potential difference is applied between two electrodes in atmospheric air, a corona discharge is induced around the thinnest electrode. For instance, positive ions are produced if a positive high voltage is applied between a needle and a plate due to the strong electric field at the surface and around the needle tip. Then, these ions are subject to Coulomb force, resulting in their motion from the active needle tip toward the grounded collecting plate. The sum of all these Coulomb forces results in a volume electrohydrodynamic (EHD) force occurring inside the discharge. Hence, many collisions exist between the positive ions in motion and neutral air atoms and molecules in the electrode gap. This results in a momentum transfer that produces a gas flow, usually called ionic wind and sometimes electric wind. Although this may sound very simple, corona discharges are the seat of highly complex physical phenomena with intense chemical activity that is difficult to understand and simulate.

Important research on the physics of corona discharges started at the end of the 19th century [1,2], and well-known researchers continued to study them mainly experimentally throughout the 20th century [3–19]. As far as ionic wind is concerned, it seems to have been first reported in 1629 by Cabeo [20]. Then, in the 18th and 19th centuries, several scientists, some very illustrious, contributed to describing the electric phenomenon. However, it was not until Harney's thesis in 1957 that the ionic wind phenomenon was explained by theory, that it was put into equations and that experimental measurements of the velocity of the ionic wind were finally carried out [21]. A few years later, Robinson published two articles describing the history of the discovery and study of the ionic wind and all the theoretical and experimental bases [22,23]. At that time, Robinson imagined that ionic wind could be used to develop gas pumps with no moving parts. Other works from this period include those by Stuezer [24], and Christenson and Moller [25]. We will not go into more detail about the history of the ionic wind,

as this is covered in one of Robinson's two articles [23]. However, Fig. 1 gives a brief overview of the key dates and the scientists who have contributed to the description and a better understanding of the phenomenon, from the 17th century up to about fifty years ago.

Since the 1980s, the ionic wind has been extensively studied for the development of ion-driven gas pumps [26–28] and its role in electrostatic precipitators [29–31], as well as for many other applications, such as cooling and thermal transfer enhancement [32], EHD drying [33], airflow control [34–36], and more recently atmospheric propulsion [37,38], to cite just a few examples of work. These main applications are presented in Fig. 2. On the one hand, it is clear that today, the ionic wind is mainly studied for its potential applications in cooling and thermal transfer, as it is undoubtedly the most promising industrial application in the short-term. On the other hand, other ways of research are essential and need to be reinforced because ionic wind could have potential applications in atmospheric propulsion for small-size drones and micro-scale ionic wind systems [39,40]. Furthermore, it could be a helpful tool for fundamental studies on flow and turbulence control as it is a simple manner to add a force and observe its effect on a flow [41]. In this case, it is more of a question of surface discharges, usually called plasma actuators.

But let us get back to the objective of this review article. It focuses on the ionic wind produced by volume atmospheric corona discharges in simple configurations with only two electrodes. The most represented geometrical configuration will be the needle-to-plate (point-plate) configuration. Still, we will also present results for other geometries, such as needle-to-ring and wire-to-plate. This means that we will not discuss the ionic wind generated by surface discharges and plasma actuators, as this will be covered in another review article, which will be published later in the Journal of Electrostatics. Moreover, we will not discuss all the electrode configurations that exist, all the applications of ionic wind, and the numerous studies that have been carried out by a lot of researchers all over the world to improve and

enhance the systems that use ionic wind, as it has already been done in two very nice and recent review papers published by Johnson and Go [42] and Qu et al [43]. Moreover, we will not discuss the numerous recent studies on atmospheric propulsion by ionic wind, which generally do not study the ionic wind itself but rather measure the total EHD force produced by the discharge using a balance. Let us be clear: in the present review article, we only aim to discuss and explain the ionic wind phenomenon. We will precisely describe its topology and explain its spatial and temporal behavior using the physical phenomena behind it.

After this introduction, the second part of the present article is devoted to the electrical properties of corona discharges. We present the behavior of the V-I characteristics, the different empirical laws that can fit them, and finally, the discharge current versus time in function of the different discharge regimes. We discuss streamers and Trichel pulses and show how the geometrical and environmental input parameters affect the discharge electrical behavior. We have chosen to present a relatively precise characterization of the discharge electrical properties, as we will see later that the behavior of the ionic wind strongly depends on them. However, readers familiar with the different regimes of positive and negative corona discharges may skip this part and go directly to the two next parts, which constitute the core of this article. Indeed, in the third part, we focus on the time-averaged properties of the ionic wind. First, we compare the mean ionic wind produced by DC positive and negative discharges from different experimental measurements. We will see that the positive discharge results in a fast, thin, and pointed jet flowing from the needle tip toward the grounded electrode. In contrast, the ionic wind jet induced by a negative discharge is usually slower and wider. The fourth part deals with the ionic wind dynamics, *i.e.* its unsteady characteristics. More specifically, we will present the role of the Trichel pulses and breakdown streamers on the ionic wind velocity versus time, and we will see that these two very fast phenomena play a key role in ionic wind production. Finally, in the fifth part, we aim to explain the behaviors

observed experimentally in parts 3 and 4, with the help of modeling and numerical simulations of the ionic wind phenomenon.

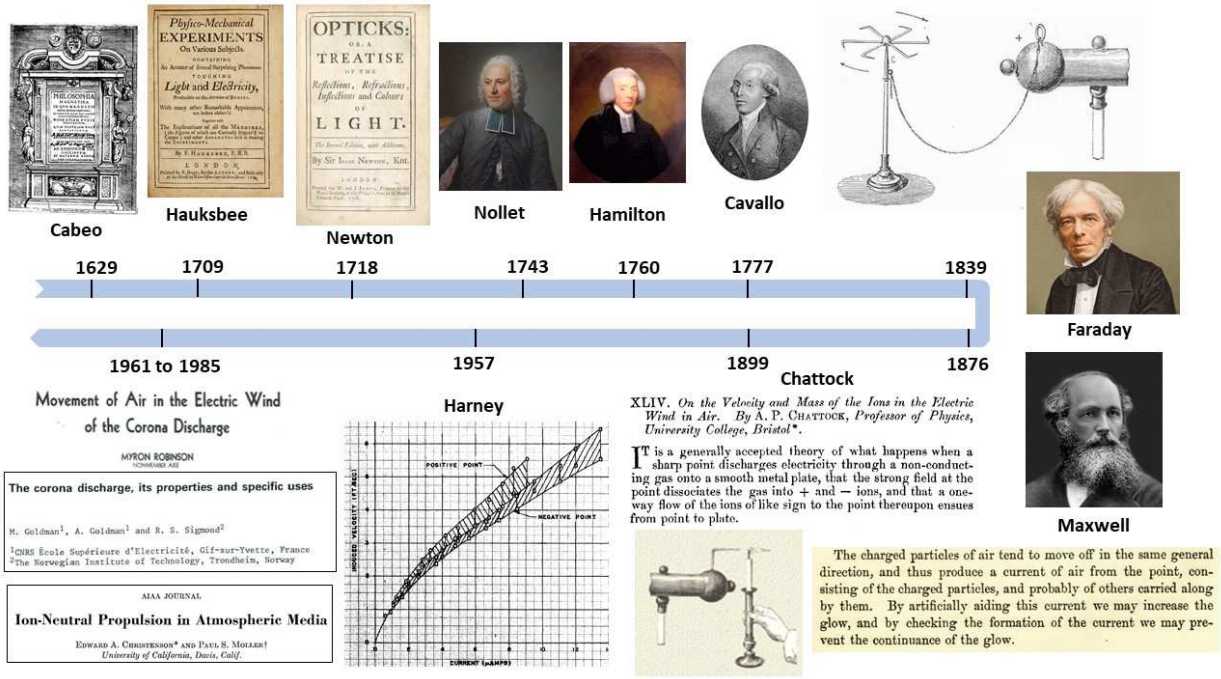

Figure 1. Key dates and main scientists who worked on the discovery of ionic wind: Cabeo [20], Hauksbee [44], Newton [45], Nollet [46], Hamilton (reported in [43]), Cavallo [47], Faraday [48], Maxwell [49], Chattock [2], Harney [21], Robinson [22], Christenson and Moller [25], Goldman et al [18]. The two drawings of the candle flame blown by the ionic wind and the electric pinwheel come from Mascart's book [50].

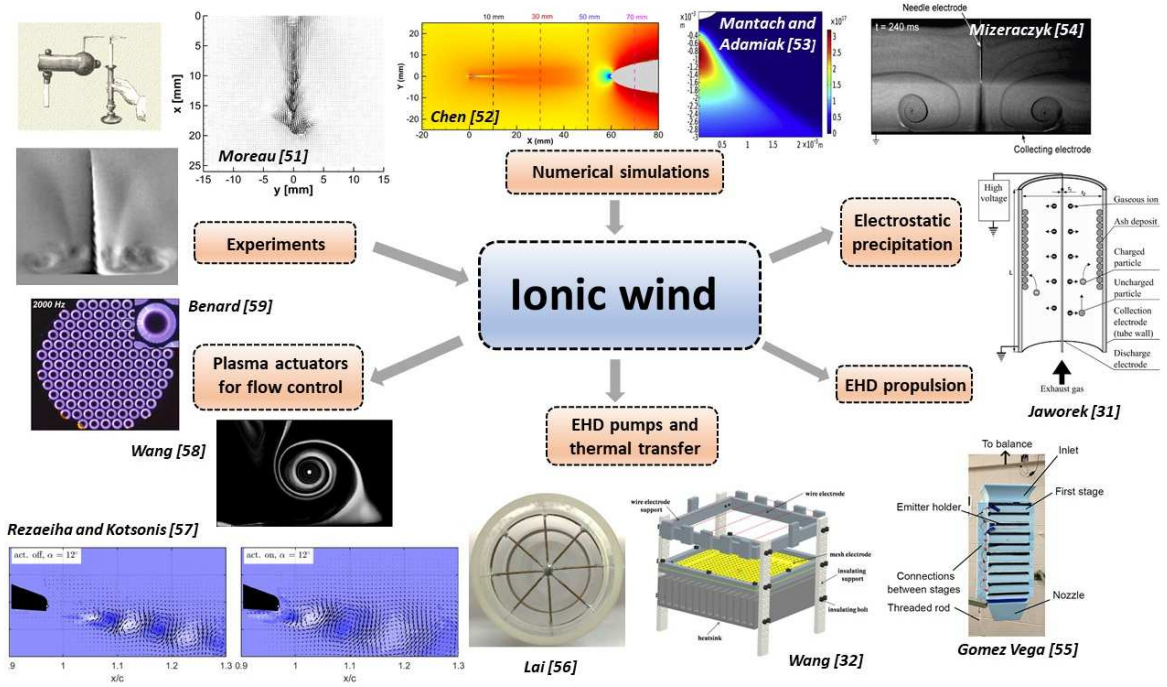

Figure 2. Illustration of ionic wind phenomenon and its main applications. Pictures come from Moreau et al [51], Chen at al [52], Mantach and Adamiak [53], Miceraczyk et al [54], Jaworek et al [31], Gomez Vega [55], Wang et al [32], Lai [56], Rezaeiha and Kotsonis [57], Wang et al [58], and Benard et al [59].

But before that, it is relevant to do a little theoretical background. From a macroscopic point of view, it is well-known that the mean electrohydrodynamic force F_{EHD} and the velocity of the resulting ionic wind V_G can be expressed as follows [60]:

$$F_{EHD} = \frac{d}{\mu} \times I \quad (1)$$

$$V_G \propto \sqrt{F_{EHD}} \quad (2)$$

with d the electrode gap, μ the ion mobility, and I the time-averaged current. These two simple expressions highlight that the total EHD force F_{EHD} increases linearly with the gap and the discharge current and that the ionic wind velocity increases with the square root of the mean current. In practice, these two expressions can be used to calculate orders of magnitude but not to represent the complex phenomenon of ionic wind. Indeed, the local EHD force f_{EHD} at a given location in the inter-electrode space depends on the space charge and the electric field at this location, varying with time. Then the total EHD force F_{EHD} is:

$$F_{EHD} = \iint_{dV} f_{EHD}(x,y,z,t)\, dV = \int_V \rho(x,y,z,t) \times E(x,y,z,t)\, dV \quad (3)$$

where the space charge is:

$$\rho = e(n_P - n_N - n_e) \quad (4)$$

This highlights that to characterize the EHD force and the ionic wind correctly, we need to know the density of electrons n_e, positive ions n_P, and negative ions n_N everywhere in space, at every time. Therefore, this is only possible through numerical simulation since these physical quantities cannot be measured experimentally. This shows that it is necessary to constantly go back and forth between experimental measurements and numerical simulations to correctly describe the ionic wind phenomenon. Experimental measurements validate theoretical models, while numerical simulations allow us to explain experimental observations and better understand the physical phenomena at the origin of the ionic wind. For this reason,

in this article, we will mainly present experimental results but attempt to explain them with the help of numerical simulations.

2. Electrical properties of corona discharges

In this part, we aim to characterize the electrical properties of volume corona discharges. First, we discuss the I-V characteristics of DC corona discharges. Secondly, we present the evolution of the current versus time as a function of the different discharge regimes for DC and AC discharges. Finally, we will discuss the role of some geometrical and environmental input parameters on the electrical behavior of these discharges.

2.1. Current-voltage characteristics

Fig. 3a shows an example of the evolution of the time-averaged current when the high voltage is gradually increased for DC positive and negative needle-to-plate corona discharges [61] (gap = 15 mm). Although a weak discharge occurs at currents below 1 µA, we usually consider that the corona discharge starts to ignite when the current reaches about 1 µA, the corresponding voltage V_0 being the onset (or ignition) voltage. In Fig. 3a, we can see that V_0 equals about ± 4 kV, whatever the polarity of the high voltage is. In the case of the negative discharge, the measurement points (red circles ●) of the I-V characteristics can be well-fitted by Townsend's law (solid red curve), which is given by:

$$I = C \times V(V - V_0) \qquad (5)$$

where V is the applied voltage, V_0 is the ignition voltage, and C is a constant depending on the electrode configuration, temperature, pressure, and gas composition. In the case of a positive discharge, the experimental I-V characteristics (blue squares ■) cannot be fitted by Townsend's law anymore (solid blue curve), but by another expression given by:

$$I = C_1 \times V^n \qquad (6)$$

with C_1 a constant different than C and n = 4 in this case (dot blue curve). This feature is interesting because it highlights that Townsend's equation is always appropriate in the case

of a negative corona but is not relevant in the case of a positive corona discharge. This point will be discussed in the next section.

In the literature, other fitting laws of the corona I-V characteristics can be found. For instance, Ferreira et al [62] introduced another expression in 1986, taken up by Meng et al. more recently [63] :

$$I = C_2 \times (V - V_0)^2 \quad (7)$$

Moreover, there are many manners to represent the I-V characteristics. We can plot I versus V with a logarithmic scale for the current to zoom on its small values, or we can plot I/V versus V [62,64] , $\sqrt{I}$ versus V [62] or V/I versus ΔV where $\Delta V = V - V_0$ [65]. For example, Fig. 3b shows the square root of I (red circles ●) and I/V (black squares ■) versus V. We can see that the evolution is linear in both cases.

Finally, three last remarks can be made. First, at a given voltage, the current is always weaker with the positive corona discharge, except in rare cases, which will be discussed later. Secondly, we can sometimes observe a hysteresis phenomenon when measuring the I-V characteristics. This results in a stronger current I when the voltage V is decreased compared to the current measured when the voltage is increased [66]. Then, decreasing the voltage to plot more reproducible I-V characteristics is more relevant. Third, the electrical power consumed by corona discharges is very low; its value is generally a few hundred milliwatt [61].

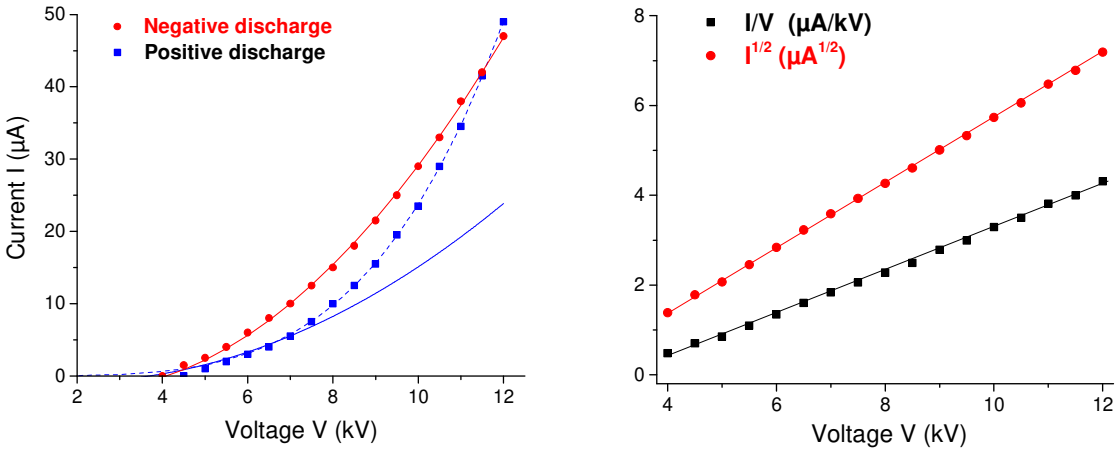

(a) (b)

Figure 3. I-V characteristics for DC positive and negative corona discharges (a) [61], other manners to represent the evolution of the discharge current versus the applied voltage, in the case of a DC positive corona discharge (b).

2.2. Discharge regimes and current versus time

First, let us consider the case of the positive corona for which the different discharge regimes have been widely described by several authors [9,10,12,13,15,16,19] and more recently by Moreau et al for a needle-to-plate design [67] and Chen at al for a needle-to-ring design [68], both these designs resulting in the same regimes (the term mode is sometimes used instead of regime). Although the nomenclature used by the researchers is not always the same, three main regimes of positive corona discharge can be observed as the voltage increases (Fig. 4a). First, when the onset voltage V_0 is reached, a burst pulse corona takes place. In this regime, the current comprises a DC component of a few µA and a pulse component of small onset streamers [68]. If the voltage is increased, this regime is replaced by the pulseless Hermstein's glow corona[69], usually called glow regime. In this case, the current is constant, and the light emitted by the discharge is located around the needle tip (Fig. 4c for + 10 kV). If the voltage is further increased, the breakdown streamer regime occurs. In this regime, we can see some luminous ionized channels (breakdown streamers) that cross the electrode gap, their number,

their thickness and their light intensity increasing as the high voltage increases (Fig. 4c for + 14 kV and + 16 kV). As a result, the discharge current is composed of a DC component (up to a few dozen of µA, depending on the electrode gap) and a pulse component (Fig. 4b). Each pulse corresponds to a breakdown streamer, itself composed of a primary and a secondary streamer [51,66,70,71]. The peak value of these pulses (from 1 mA to a few dozen mA), their frequency (a few kHz) as well as the energy and the electrical charge of each pulse, increase with the applied voltage (Fig. 4d). Moreover, when the electrode gap is decreased, the magnitude of the current pulses and their frequency increase [66].

Let us return to Fig. 3a, still in the case of a positive corona discharge. On the one hand, up to +7 kV, the measured discharge current is consistent with Townsend's law because the discharge regime is the glow one. On the other hand, from +7.5 kV, the measured current is higher than that predicted by Townsend's law. This is due to the change in the discharge regime, which transitions from the glow to the breakdown streamer regime. Indeed, from +7.5 kV, the current versus time is composed of a DC component plus a pulse component corresponding to the current carried by the streamers. Consequently, we can assume that Townsend's law is relevant for the glow regime but not for the breakdown streamer regime.

Note that two other regimes may sometimes be observed. First, after the breakdown streamer mode, a pulseless diffuse corona regime can occur before a spark takes place. Second, Yan et al. recently highlighted a new regime between the glow regime and the breakdown streamer one [66]. In this regime, the authors could observe streamers that do not cross the entire electrode gap, with properties different than those of breakdown streamers (magnitude around 1 mA and frequency of about 20 kHz). The authors have considered that this new regime, which had never been reported before, was due to the oxidation of their commercialized tungsten needle.

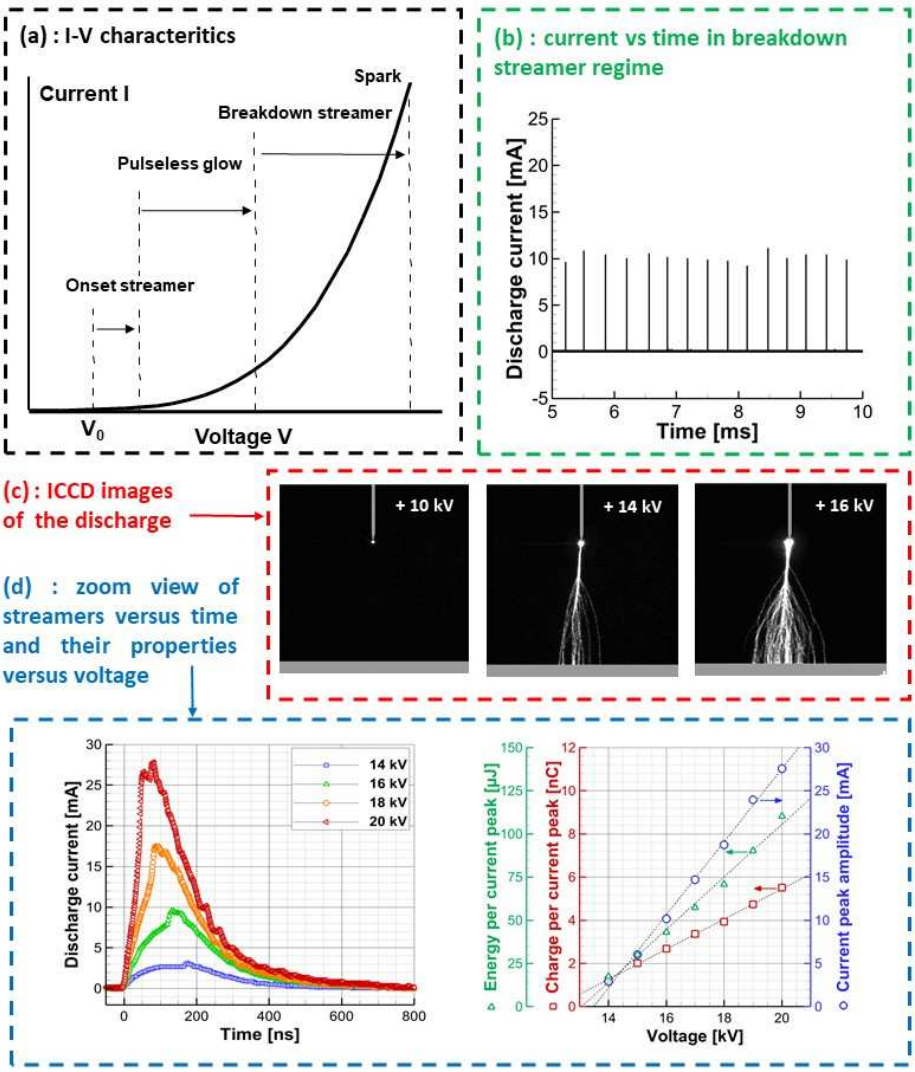

Figure 4. Different regimes of the DC positive corona discharge [51].

Now, let us look at what happens in the case of a negative discharge. With a negative polarity, different regimes have also been reported in the literature, often by the same authors than for the positive coronas, even if it is well-known that Trichel worked a lot on negative coronas [7]. Hence, when the discharge ignites, we first have a Trichel pulse corona, and then a pulseless corona before the transition to spark. Fig. 5a presents an example of current versus time in the case of Trichel regime, with each current pulse corresponding to a Trichel pulse. These current pulses have a duration of a few hundred nanoseconds, a magnitude of a few hundred µA, and a frequency of a few hundred kHz (up to MHz). Their

magnitude does not depend on the applied voltage, whereas their frequency increases when the voltage is higher and the electrode gap is smaller [72,73]. Fig. 5b shows photographs of the light emitted by the negative discharge in Trichel regime (left) and pulseless regime (right) [68]. They highlight that the discharge activity is confined around the needle tip, regardless of the regime. Several other works have verified this. This point will be more precisely discussed later in this article, but we can already say that the physics of this phenomenon has nothing to do with that of the positive breakdown streamer.

The different discharge regimes described above are observable in the case of needle-to-plate and needle-to-ring corona discharges. However, if the geometrical configuration of the discharge is changed, some of these regimes do not occur. For instance, in the case of wire-to-plate and wire-to-cylinder designs, the positive breakdown streamer regime is rarely observable (the discharge directly transitions from the glow discharge to the spark), and the discharge is confined around the wire [74]. In the case of a negative Trichel regime, the discharge is not homogeneous along the wire but is composed of several spots regularly distributed along the wire [74].

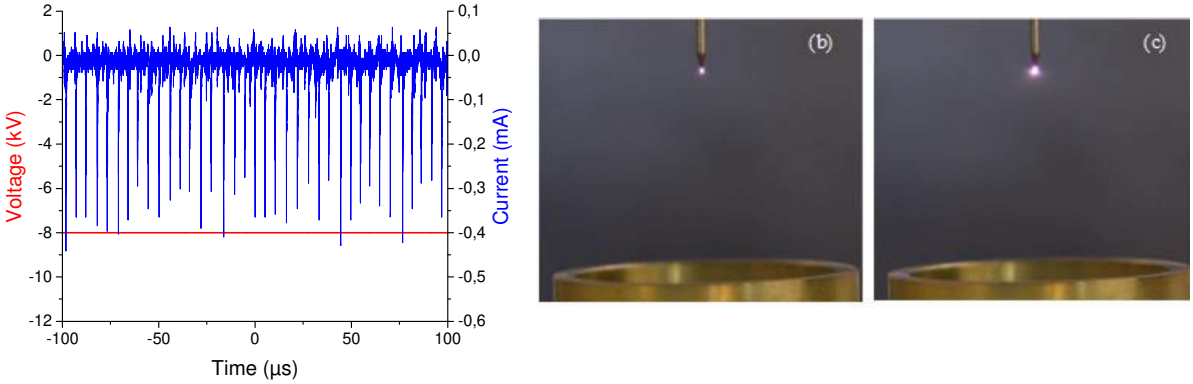

Figure 5. Current versus time in the case of a DC negative corona discharge (Trichel regime) [61] and pictures of a negative corona discharge in Trichel regime (left) and pulseless regime (right) [68].

To conclude, there is one last point to comment on. It also concerns Fig. 3a. On this I-V characteristics, we can see that the negative current is always higher than the positive one, at least up to ± 12 kV. We can legitimately wonder why. We will provide a simple answer here, but we will explain this point in more detail in the conclusion of this article. In the case of the negative needle-to-plate corona discharge, the phenomenon of electron avalanche leads to the formation of positive ions in a region very close to the needle tip (ionization region), which drift rapidly toward the negative active needle. Then, negative ions produced by attachment drift toward the plate, as well as electrons. The negative current is then due to the motion of negative ions and electrons in the drift region. In the case of a positive glow corona discharge, the electron avalanche forms positive ions by ionization, which drift toward the plate, and electrons that move toward the needle tip. In the drift region, the electron density is weak, and the current is thus mainly due to the motion of positive ions. This could explain why the positive current is smaller than the negative one. However, when the breakdown streamer regime occurs, a pulse current is added to the DC current, resulting in a significant rise in the mean positive discharge current. Then, the mean measured current diverges from Townsend's law, as it is highlighted by Fig. 3a. As the voltage increases further, the frequency and amplitude of the streamers increase, and the total current also increases. This is why the positive current amplitude exceeds the negative one above ± 12 kV.

2.3. AC corona discharge

The DC voltage can be replaced by an AC voltage (with no DC component) with different waveforms to ignite a corona discharge [75,76]. Then, the current is composed of a synchronous component (corresponding to the DC component of a few μA in the case of a DC corona discharge), plus eventually a pulsed component, depending on the discharge regime. For instance, Fig. 6a shows an example of the current versus time (in blue) in the case of a 15-mm-

gap needle-to-plate corona discharge powered by a sine high voltage (voltage magnitude V_{AC} = 12 kV and frequency f_{AC} = 200 Hz) [75]. We can see that two different discharges occur, one during the positive half-cycle and another during the negative half-cycle of the voltage v(t). More precisely, if we start our observation at t = 0, we can see six current pulses between t = 0.75 and t = 1.5 ms, their peak value and frequency being around 5 mA and 5 kHz, respectively. In this time range, the discharge regime is thus the breakdown streamer regime, with a voltage greater than + 9 kV. However, we cannot see the synchronous current because it is too small (a few µA) compared to the current scale of Fig. 6a. Furthermore, we can think that when the voltage v(t) is smaller than +9 kV (and above the onset voltage), a glow corona discharge occurs, but it is not observable in Fig. 6 because the current scale of the y axis is too high. During the negative half-cycle, Fig. 6a shows many small current pulses. Still, they are difficult to see because their magnitude is weak compared to the scale of the y-axis. Therefore, Fig. 6b presents a zoomed view of these current pulses (here, V_{AC} = 8 kV at a frequency f_{AC} of 100 Hz). These pulses correspond to Trichel pulses with a magnitude of about 0.15 mA and a frequency depending on the value of the instantaneous voltage v(t), ranging between 100 kHz and 500 kHz in this case.

To conclude, we can say that when a corona discharge is powered by an AC voltage, a positive corona discharge takes place during the positive half-cycle, and a negative discharge occurs during the negative half-cycle, with roughly the same properties as the DC corona discharges. Between these two discharges, when the instantaneous voltage v(t) is smaller than the onset voltage, there is no discharge. Moreover, the electrical power consumption of AC corona discharges is similar to that of DC corona discharges.

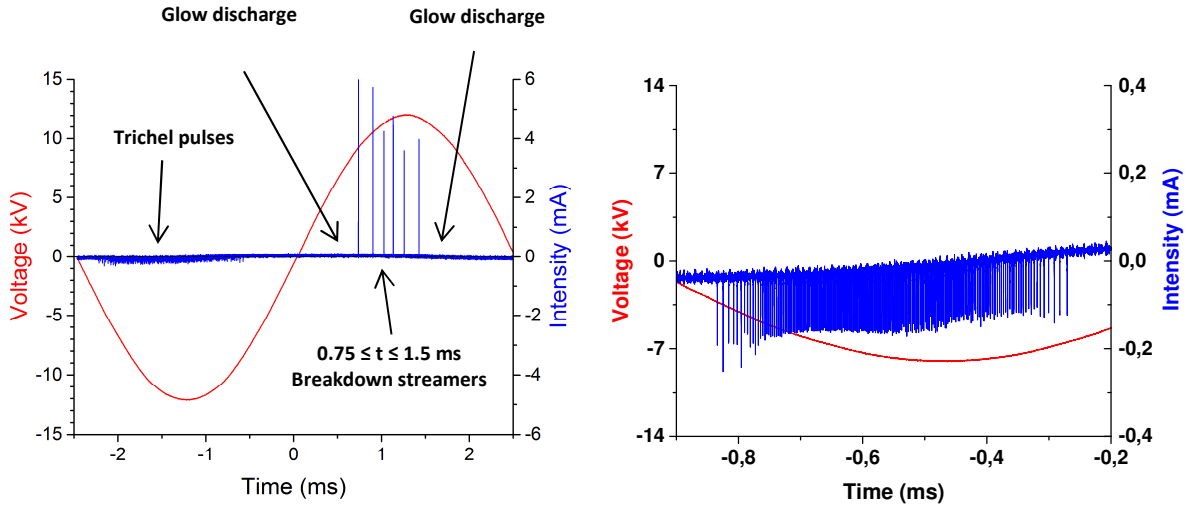

(a) (b)

Fig. 6. Current versus time for a corona discharge powered by a sine high voltage (voltage magnitude V_{AC} = 12 kV, frequency f_{AC} = 200 Hz) (a), zoom view of the Trichel pulses during the negative half-cycle (V_{AC} = 8 kV, f_{AC} = 100 Hz) (b). Data from [75].

2.4. Influence of input parameters

Of course, the discharge physics and the resulting current depend on numerous electrical, geometrical, and environmental input parameters. Concerning the electrical parameters, we have already discussed that the voltage plays an important role in the time-averaged current, and on the frequency of streamers and Trichel pulses. In fact, at a given electrode gap, the discharge regime depends on the voltage value. We also indicated the role of the gap on the frequency of streamers and Trichel pulses. Furthermore, we know that the onset voltage V_0 is smaller when the curvature radius of the needle or the wire is decreased [77]. Thus, for the same voltage, the discharge current is higher.

Concerning the environmental parameters, it is clear that they play a key role in the discharge physics. Without precisely discussing the effect of each of these parameters on the electrical properties of corona discharges, we can indicate, for instance, that (1) the relative humidity of the surrounding air results in a change in the I-V characteristics as it modifies the onset voltage and the dynamics of streamers and Trichel pulses [78,79], (2) the temperature does not significantly influence the discharge [80], (3) the pressure is a fundamental input parameter and, as for all the types of discharge, the current is fully increased when the pressure drops [80],

(4) the nature of the surrounding gas plays a key role in the corona discharge physics [81], (5) the presence of an external airflow on the corona discharge results in substantial modifications of the current [82] and of the properties of streamers [83]. This list is not exhaustive, as the individual effect of environmental input parameters is not the focus of the present article.

3. Time-averaged ionic wind

In this part, we aim to discuss the time-averaged properties of the ionic wind produced by corona discharges. First, we discuss the link between the average ionic wind velocity and the applied voltage. Secondly, we present different experimental results on the time-averaged velocity fields of the ionic wind produced by needle-to-plate and needle-to-ring corona discharges. Finally, we discuss the effect of some electrical, geometrical, and environmental input parameters.

3.1. Ionic wind velocity versus applied voltage

Fig. 7a presents the time-averaged velocity of the ionic wind measured with a hot wire anemometer probe downstream of a needle-to-ring corona discharge as a function of the applied voltage value for both negative and positive polarities. This curve, coming from the work of Chen et al. [68], leads to two main comments. First, it shows that the ionic wind average velocity increases approximately linearly with the potential difference applied between the two electrodes. Secondly, from about ± 14 kV, the velocity produced by the positive discharge is slightly higher than the one induced by the negative discharge. Fig. 7b presents the maximum velocity of the ionic wind measured with a Pitot tube at several distances downstream of a positive (left) and a negative (right) needle-to-ring corona discharge as a function of ΔU (ΔU corresponding to the applied voltage V minus the ignition voltage V_0, *i.e.* $\Delta U = V - V_0$). This work of Zhang et al. [65] confirms the two previous comments, and it brings new information: the maximum velocity, measured here in front of the needle tip, increases

linearly with the applied voltage and more, it is significantly higher with the positive corona discharge. This is all the more surprising given that we know that at the same voltage value, the negative discharge current is higher. This means the positive current is more efficient than the negative current at producing ionic wind. We will come back later on this feature and explain why.

To conclude the link between the ionic wind velocity and the applied voltage, we can assume that the wind velocity increases approximately linearly with the voltage, as confirmed numerically and experimentally by other authors [27,84]. In addition, this result agrees with the theory, which indicates that the ionic wind velocity V_G is proportional to the square root of the mean current I (equations 1 and 2) and that the current I is proportional to the square of the applied voltage V (equation 5), leading to a linear relationship between V_G and V. This has been clearly demonstrated by Guan et al. [85] with an analytical model. Moreover, based on the work of Drews et al. [86], Zhang et al. [65] proposed a simplified expression of the ionic wind velocity that confirms this tendency:

$$V_G = \sqrt{\frac{\varepsilon_0}{\rho}} \times \frac{\Delta U}{d}$$

where ε_0 is the air permittivity, ρ is the air density, d is the electrode gap and ΔU is equal to the applied voltage minus the onset voltage ($\Delta U = V - V_0$).

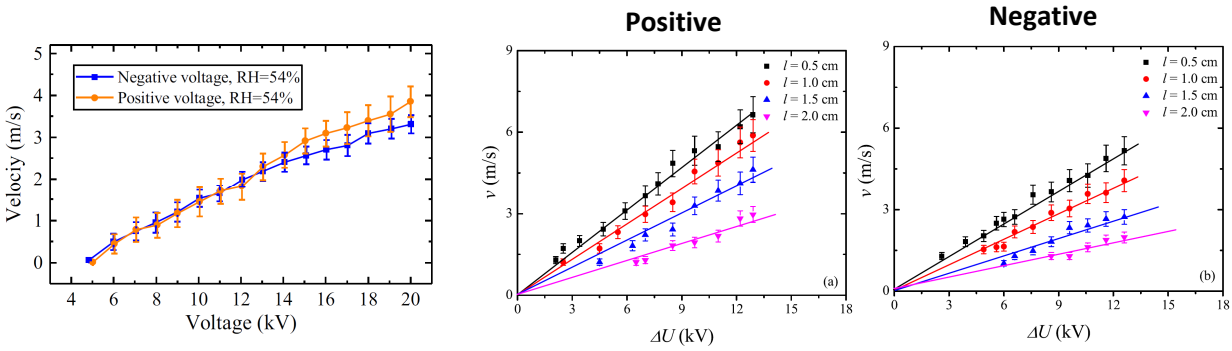

(a) (b)

Fig. 7. Mean velocity of the ionic wind measured downstream of positive and negative needle-to-ring corona discharges versus the applied voltage [68] (a) and maximum ionic velocity measured downstream of positive (left) and negative (right) needle-to-ring corona discharges versus the applied voltage $\Delta U = V - V_0$ [65] (b).

3.2. Velocity fields and velocity profiles

Fig. 8 presents velocity fields of the ionic wind induced by DC positive (left) and negative (right) needle-to-plate corona discharges obtained from particle image velocimetry (PIV) measurements [67]. In these experiments, the needle tip is located at x = 0 and y = 0 when the plate is located at y = 25 mm (gap = 25 mm).

Several remarks can be made. First, we can see that the ionic wind consists of an air jet, flowing from the needle tip toward the plate. Secondly, these velocity fields are two-dimensional, whereas the ionic wind jet is three-dimensional. In practice, the jet is cone-shaped, and it should be, in theory, axisymmetric with respect to the x = 0 axis. However, quite often, the jet is not perfectly perpendicular to the plate, for example, when there is a geometric defect at the tip or when the angle of the needle with the plate is not perfectly equal to 90 degrees. Third, the polarity of the applied voltage significantly influences the topology of the ionic wind.

On the one hand, for the negative corona, the maximum velocity is concentrated in a region close to the tip. This region grows and spreads progressively toward the plate when the high voltage increases. Moreover, the velocity decreases along the vertical x-axis, even at

- 16 kV, meaning that the electrohydrodynamic (EHD) force occurs mainly close to the tip. Consequently, when one moves away from the needle, the ionic wind velocity decreases because of viscous effects. On the other hand, the voltage effect is fully different for the positive corona discharge. Up to + 12 kV, the region of maximum velocity is located near the needle tip, as for the negative discharge. However, from + 14 kV, the mean velocity becomes constant along the x-axis, meaning there is still an EHD force in the inter-electrode gap. In their paper, the authors [67] explained that this sudden increase in the velocity above + 14 kV is due to the transition from a glow discharge (at + 12 kV) to a breakdown streamer discharge (at + 14 kV), highlighting the key role of breakdown streamers on the electrohydrodynamic force and the resulting ionic wind.

This is confirmed by Fig. 9, which presents velocity profiles along y, at x = 12.5 mm (half distance between both electrodes), obtained from the velocity fields of Fig. 8. On the one hand, these profiles highlight that the velocity of the ionic winds produced by the negative and positive corona discharge are rather similar up to ± 12 kV, even if we can assume that the velocity is slightly smaller with the negative discharge. The jet is slightly more expansive with the negative discharge, and the jet induced by the positive discharge has a pointed shape. On the other hand, from + 14 kV, the maximum velocity (in front of the needle tip) induced by the positive discharge suddenly rises from about 3.7 m/s to almost 8 m/s, showing that breakdown streamers significantly improve the production of ionic wind. This feature will be discussed and explained later in this article.

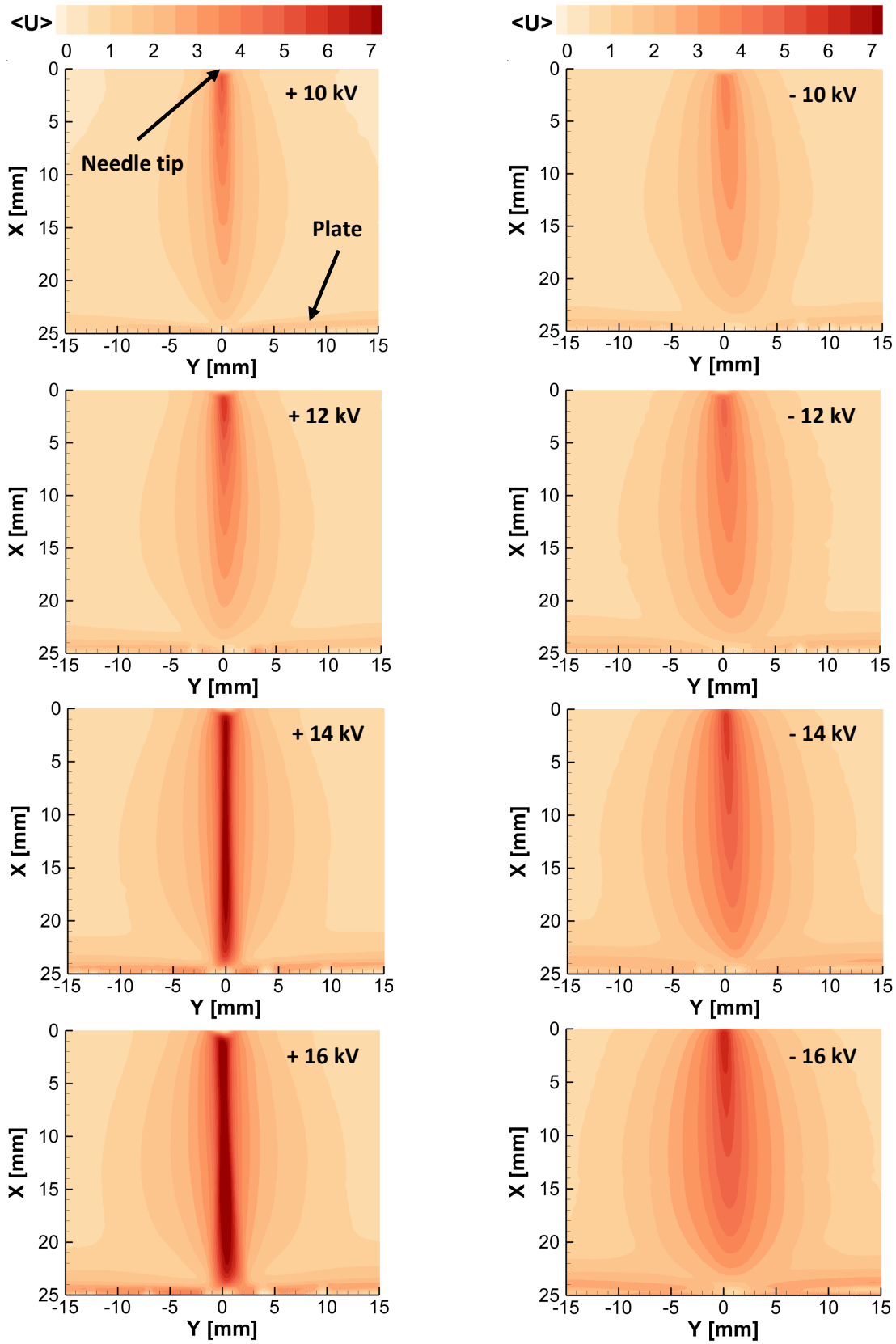

Fig. 8. Velocity fields for needle-to-plate DC positive and negative corona discharges for different voltage values [67]. The needle tip is at x = 0 and y = 0 when the plate electrode is at x = 25 mm.

To conclude, we can assume one more time that the positive discharge is more efficient at producing ionic wind. If we compare the positive and negative discharge at ± 12 kV, the positive ionic wind is much higher than the one produced by the negative discharge whereas the positive and negative currents measured in this study equaled + 20 µA and – 33 µA, respectively [67].

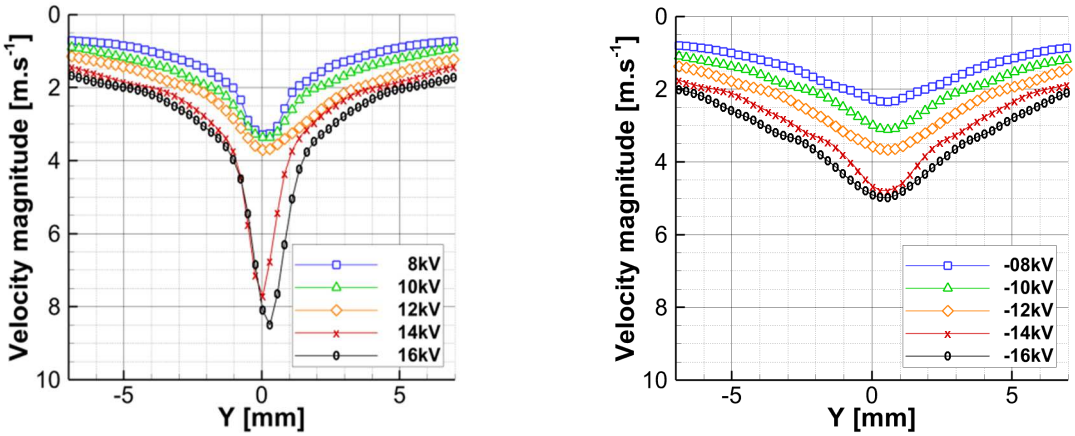

(a) (b)

Fig. 9. Velocity profiles at x = 12.5 mm for positive (a) and negative (b) needle-to-plate corona discharges [67].

The article from which the two previous figures are taken (Fig. 8 and 9), published in 2018 [67], is not the only one to have evidenced this behavior. For instance, the same research team had already shown this phenomenon in 2008 [87], as illustrated by Fig. 10a. Indeed, Fig. 10a presents profiles of the velocity measured with a Pitot tube at 2 mm downstream of a needle-to-grid corona discharge for negative (red circles ●) and positive (black squares ■) voltages. This figure shows that the velocity is similar with both polarities, except in front of the needle tip located at y = 0, where the positive discharge results in a higher velocity. The authors had already indicated that this feature was certainly due to the presence of breakdown streamers in the case of the positive corona discharge. A few years later, Zhang et al. [65] confirmed this behavior (Fig. 9b). Finally, the numerical simulations and the

experimental measurements of Guan et al. in 2018 [84] also highlighted an over-velocity in front of the needle in the case of a positive corona discharge (Fig. 9c). Thus, there is no doubt on this feature: the velocity in front of the needle tip is higher in presence of breakdown streamers [88]. The ionic wind jet induced by a positive discharge is faster and sharper than the one resulting from a negative discharge when the discharge regime is the breakdown streamer one.

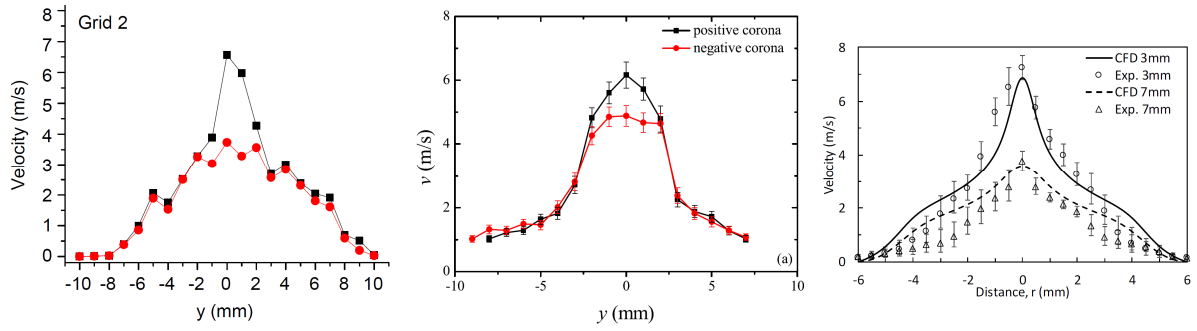

(a) (b) (c)

Fig. 10. Velocity profiles of the ionic wind measured downstream of a needle-to-grid configuration for positive (black square ■) and negative (red circles ●) corona discharges [87] (a), velocity profiles of the ionic wind measured downstream of a needle-to-ring configuration for positive and negative corona discharges [65] (b) and velocity profiles of the ionic wind downstream of a needle-to-ring configuration for a positive corona discharge [84] (c).

Concerning the width of the ionic jet, in addition to the study of Moreau et al. [67], several other works compared the velocity profiles of the ionic wind produced by positive and negative corona discharges. Among them are those of Ashikhmin et al. [89] and Zhang et al. [90] (Fig. 11). Fig. 11a presents ionic wind velocity profiles at several voltages for positive (on the left) and negative (on the right) polarities in a needle-to-ring configuration [89]. The electrode gap equals 24 mm, and the ring internal diameter is 8 mm. These experimental PIV measurements clearly highlight that in this configuration, the positive ionic wind jet is faster and more pointed than the negative ionic wind jet. For instance, if we compare the two cases at +13.6 kV and - 13.8 kV (these two values are very close), the maximum velocity exceeds

11 m/s for the positive corona discharge when it is limited to 6 m/s for the negative one. To be honest, this big difference is surprising as a difference of such magnitude between positive and negative ionic winds has never been reported in other studies. We will see later that it is due to the geometry of the electrodes. Anyway, on the one hand, there is no doubt that the positive ionic wind is faster than the negative one. On the other hand, the difference in the jet width is unclear, as the positive and negative jets seem to have roughly similar widths.

On the contrary, Fig. 11b clearly shows that the jet produced by the negative corona discharge is much slower (the velocity ranges in the y-axis that corresponds to the velocity are not the same for both figures) and wider than the jet induced by the positive discharge. For instance, let us consider the case for which ΔU is equal to 12 kV ($\Delta U = V - V_0$, corresponding in practice to V equal to +19 kV and -18 kV for the positive and negative discharges, respectively). If we look at the velocity at y = 10 mm, we can see that it is around 1 m/s for the negative jet and around 0.5 m/s for the positive one. This shows that the negative ionic wind jet is wider than the positive one.

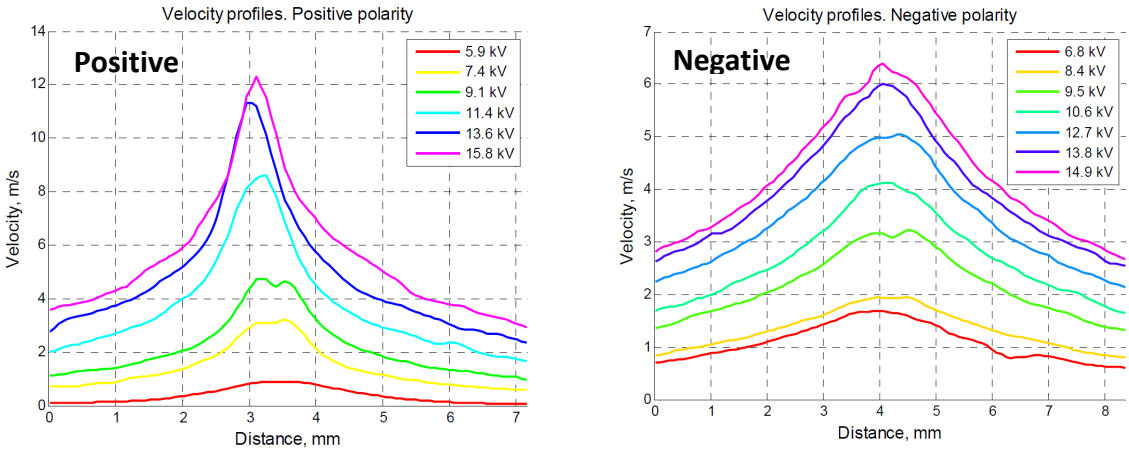

(a)

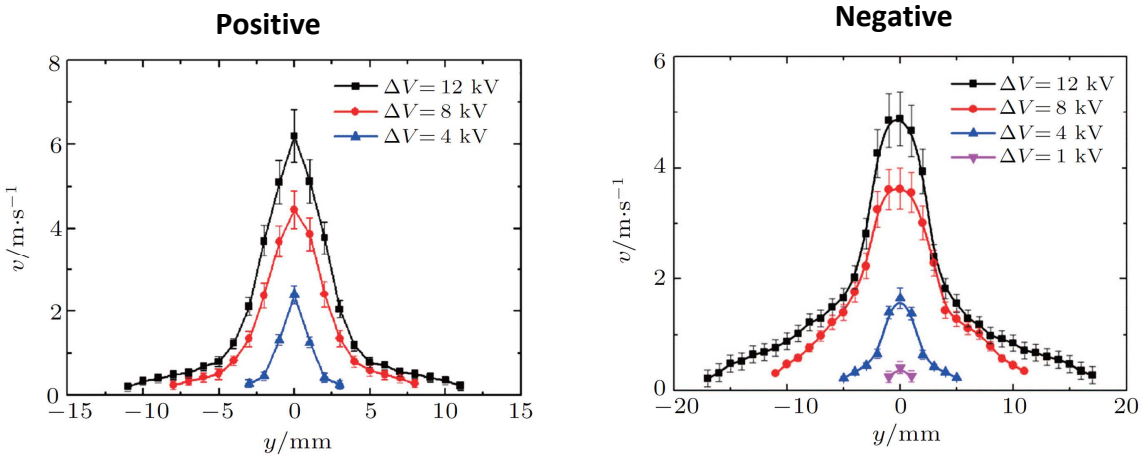

(b)

Fig. 11. Velocity profiles of the ionic wind in a needle-to-ring configuration for positive (on the left) and negative (on the right) corona discharges (a) [89], and experimental velocity profiles of the ionic wind measured 5 mm downstream of needle-to-ring positive and negative corona discharges (b) [90].

The question is, then, why does the study of Zhang et al. [90] clearly shows that the negative ionic wind jet is wider when it was not the case in the study of Ashikhmin et al. [89] ? The main reason is the geometry of the corona discharge setup. In the work of Ashikhmin et al., the electrode gap is equal to 24 mm, and the internal diameter of the ring is 8 mm. Then, the propagation of the discharge is limited in width, and the ion drift zone is longer than it is wide. Consequently, this geometry results in a concentration of the discharge in front of the needle tip. Thus, this leads to a thin jet with a pointed shape for the two polarities. It may be the reason why Ashikhmin et al. measured such a high velocity in the case of the positive discharge because the breakdown streamers are concentrated in front of the needle tip. On the contrary, in the work of Zhang et al. [90], the discharge is ignited between a needle and a ring whose internal diameter equals 30 mm, and the electrode gap equals 20 mm. In this configuration, the discharge propagates and expands in width, and less in the direction of the needle. This results in a slower jet whatever the polarity is, and above all, the ability for the negative jet to propagate in width. Consequently, we can assume that when the geometry allows, the negative discharge can propagate more widely, and the ionic wind jet is then wider.

Let us now have a look at the evolution of the ionic wind velocity between the active and the collecting electrodes, in the x direction. In practice, there is very little data in the literature on the evolution of the ionic wind velocity in this direction. Indeed, researchers usually prefer to plot velocity profiles along y, such as in Fig. 8, 9, 10, and 11. That being said, Fig. 12 presents two examples. In Fig. 12a, we can see the velocity profile in front of the needle, from its tip toward the collecting plate [61]. The needle tip is located at x = 0 and the plate electrode at x = 15 mm, the gap being equal to 15 mm. At x = 0, at the wall of the needle tip, the velocity is equal to zero. Then, it rapidly increases to reach a stable value. As we get closer to the plate, the velocity suddenly decreases and finally reaches zero at the plate wall. Fig. 12b shows a numerical simulation of the EHD force and the resulting velocity in the case of a corona discharge ignited between a wire and an airfoil [52]. This figure is very educational, as it clearly shows that the EHD force is maximum at the wire, reaching 10 000 N/m^3. This makes sense since this is where the electric field and the space charge are maximum (see equation 3). Then, the force decreases rapidly in the inter-electrode zone, down to about one hundred N/m^3. Finally, very close to the edge of the airfoil, the EHD force increases a little because the small curvature radius of the airfoil certainly results in a weak ionization phenomenon at its wall. Concerning the velocity profile (in blue), it is similar to the experimental one presented in Fig. 12a.

The profiles of Fig. 12 are examples. However, the behavior of this type of profile depends on the distribution of the electrohydrodynamic force in space and, thus, on the geometry of the electrodes and the applied voltage. For instance, if the ion density in the drift zone is weak, the EHD force cannot counter the viscous effect, and then, after reaching the maximum velocity within a few millimeters of the tip, the velocity gradually decreases. On the

contrary, the velocity can increase with x if a sufficient space charge is present in the drift region.

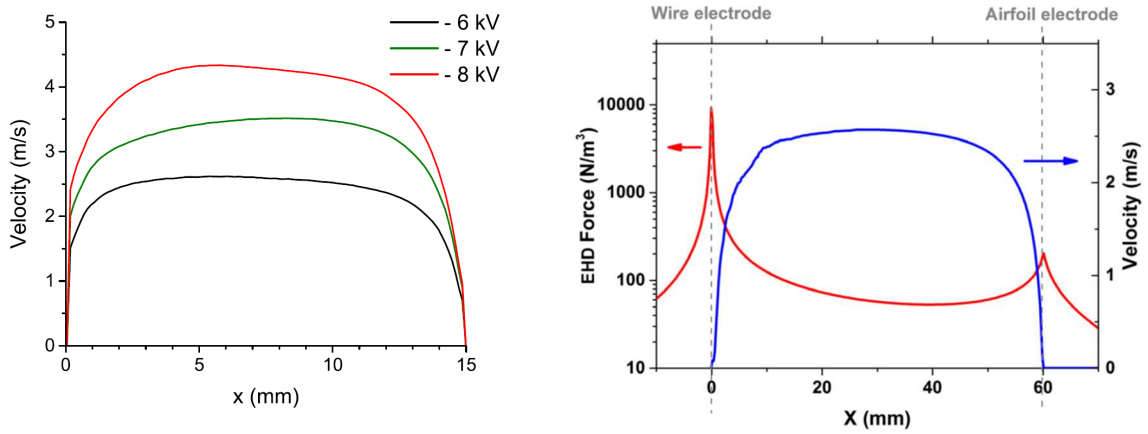

(a) (b)

Fig. 12. Experimental velocity profile in front of the needle tip, in the case of a 15-mm gap needle-to-plate negative corona discharge [61] (a), numerical velocity profile and EHD force distribution between an active wire and a collecting airfoil electrode [52] (b).

Finally, to conclude this section, we need to address one last point: even if the positive corona discharge usually results in a faster ionic wind, there are some cases where this is not true. The first example is the study of Defoort and Moreau [61]. The authors obtained a faster ionic wind with a negative corona in this experimental work. We can obviously ask ourselves why. The answer is undoubtedly that the voltage values were very low, that the positive discharge was in the glow regime, and that the positive current values were very low compared to the negative current. Indeed, the negative current was twice as great as the positive current. This was confirmed by another study [91]. In this study, which uses a 5-mm-gap needle-to-plate geometry, the ionic wind jets produced by positive and negative corona discharges were compared. The voltage ranges from ± 3.5 kV up to ± 5 kV. At ± 3.5 kV, the negative ionic wind (≈ 3 m/s) was strongly faster than the positive one (≈ 1.5 m/s). On the contrary, from ± 4.5 kV, the positive ionic wind velocity (≈ 6 m/s) was higher than the velocity

produced by the negative discharge (4.5 m/s). The last example is the one of Yang et al [92]. In their article, the authors measured a faster negative ionic wind, but one more time, the applied voltages (± 4 kV) were very low compared to the electrode gap (20 mm). We cannot explain in detail why, because the physical phenomena are very complex and very different depending on the discharge polarity, but it seems that the ionic wind produced by the negative discharge can be faster than the positive one at a given voltage value only when the value of the applied voltage magnitude is weak.

3.3. Influence of input parameters

The topology and the intensity of the ionic wind produced by a corona discharge evidently depend on electrical, geometrical, and environmental input parameters. In this section, we briefly discuss the effects of some of them.

Concerning the electrical parameters, we have seen that the value and the polarity of the applied high voltage are key parameters of the ionic wind produced by DC corona discharge. However, this type of discharge can be powered by an AC voltage. Let us start with the effect of this input parameter. In 2013, Drews et al. [86] investigated the ionic wind produced by a needle-to-ring corona discharge placed inside a tube (Fig. 13), and compared DC and AC discharges. As an example, Fig. 13 presents the ionic wind velocity as a function of the frequency of a sine high voltage, for several RMS voltage values. This figure highlights that the velocity increases with frequency up to about 500 Hz. For higher frequencies, there is a saturation effect and the velocity does not increase anymore.

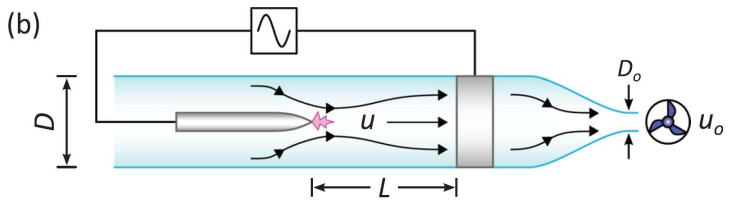

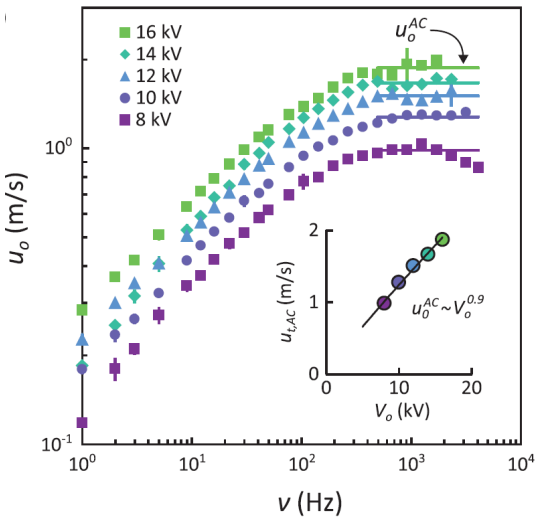

Fig. 13. Sketch of the corona discharge setup used by Drews et al. [86] and measured velocity versus voltage frequency, for several RMS voltage value. The gap is equal to 10 cm.

In 2022, Moreau and Defoort published two articles on the characteristics of the ionic wind induced by corona discharge powered by an AC sine high voltage [75] and with different AC voltage waveforms [76]. In these studies, on the one hand, the authors highlighted that the time-averaged behavior of the ionic wind jet was roughly similar to the one observed in the case of a DC discharge. On the other hand, the behavior of the ionic wind versus time is fully different, but this point will be discussed in the fourth part entitled “Ionic wind versus time.”

From an average ionic wind point of view, the results of both these studies show some interesting features. First, in the case of a sine high voltage, it has been demonstrated that the velocity increases with both the magnitude and frequency of the applied voltage. Second, the jet thickness increases with the voltage, whereas it remains constant when the frequency is increased. Third, the voltage waveform plays a key role in the ionic wind jet. For instance, Fig. 14 presents two time-averaged velocity fields, one in the case of a sine voltage and another one in the case of a square voltage (voltage magnitude of 14 kV and frequency of 500 Hz in the two cases). In these pictures, the needle tip is located at x = 0 and y = 0, and the plate covered by a dielectric is placed at x = 15 mm. Then, in this figure, the ionic wind flows

from the left to the right. As we can see, the ionic wind produced with the square high voltage flows much faster. This is because the physics and the electrical properties of the two discharges are very different, as well as the dynamics of the EHD force. For more details, we recommend readers to consult the original article [76].

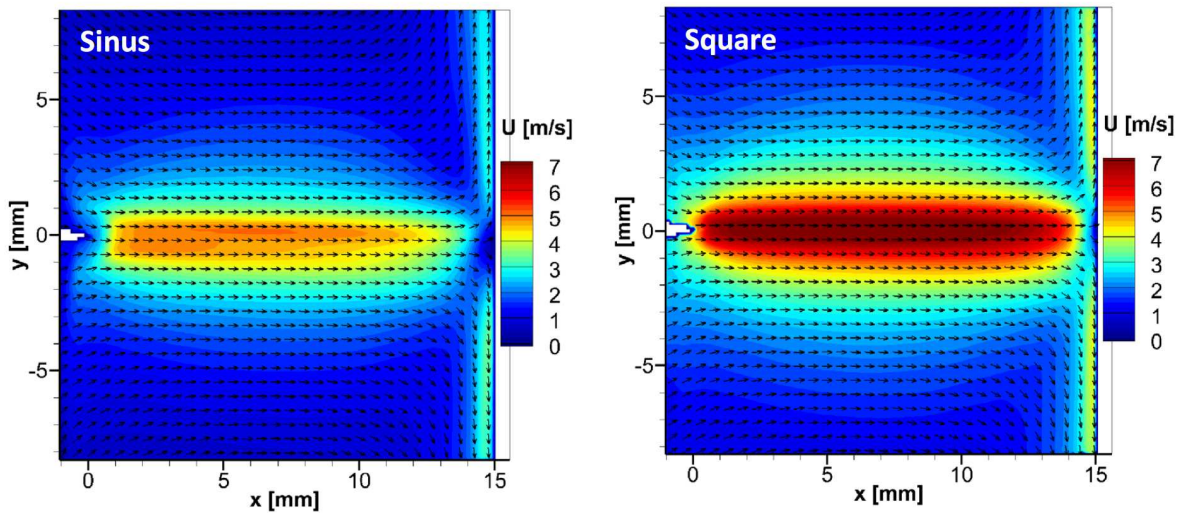

Fig. 14. Velocity fields of the ionic wind produced by a 15-mm gap needle-to-plate dielectric barrier corona discharge powered by two different high voltage waveforms: sine and square [76]. In these pictures, the needle tip is located at x = 0 and y = 0, and the plate covered by a dielectric is placed at x = 15 mm. For the two cases, the voltage magnitude is equal to 14 kV and the frequency is 500 Hz.

Concerning the influence of geometrical parameters, we consider the designs composed of only two electrodes in this article. Indeed, if we had decided to make a summary of all the geometrical configurations that exist, it would be like doing a review, such as the ones of Johnson and Go[42] and Qu et al [43], and it is not the objective of the present article. Therefore, we only consider the cases for which the corona discharge is ignited around a needle or a wire, and the collecting electrode is a plate, a ring or a grid.

First, we have already discussed the effect of the shape and the size of the collecting grounded electrode. They affect the ionic wind as they modify the electric field distribution in space, and potentially the electric field line around the needle tip. It is also well-known that the curvature radius of the active electrode plays an important role as the electric field is

higher at the needle tip when the curvature radius is smaller, and then the current also. However, the effects of two other input parameters are less known: the angle of the needle in comparison to the collecting electrode (we call it β) and the tip angle (α). It is the reason why it is interesting to discuss these two parameters.

Concerning the first parameter β, Elagin et al. [93] investigated it experimentally in the case of a positive discharge, for angles β equal to 0, 45, 60, and 90 degrees. Measurements were carried out with a laser Doppler velocimetry system (LDV). The design comprised a needle and a plate, spaced by 20 mm. Fig. 15a and 15b present the ionic wind distribution for β = 0 and 45°. Surprisingly and non-trivially, we can see that the ionic wind follows the needle angle. In their article, the authors showed that even at β = 90°, the angle of the ionic jet was about 80 degrees. That is said, that makes sense. Indeed, the ionic wind is mainly due to the high EHD force at the close vicinity of the needle tip (see Fig. 12b) and not to the force and the motion of ions in the drift zone, as many people think and as it is often explained. Indeed, close to the tip, the electric field lines follow the angle of the needle, especially if the plate is far away, and the EHD force too. Three years later, in 2020, the same research team conducted numerical simulations, which confirmed their experimental results [94]. Finally, a recent study of Moreau et al. showed that it was also the case for small gaps, down to 2.5 mm [91] (Fig. 15c).

To our knowledge, there is no experimental study about the effect of the tip angle or the tip shape (excepted the curvature radius). It is the reason why it is interesting to let readers know the results of the article of Rubinetti et al. [95] as they are surprising and not trivial. In this article, the authors conducted numerical simulations of the ionic wind produced by a needle-to-plate corona discharge ignited inside a closed ring (see the original article to have the exact geometry), and they investigated the effect of the tip angle on the induced ionic wind (the tip angle α is defined by the scheme of Fig. 16). Fig. 16 shows two examples of velocity fields, for

a tip angle α equal to 10 and 70 degrees. The difference between the two cases is very important. At α = 70° (short tip), the velocity is limited to about 1 m/s when it reaches 5 m/s with a tip angle of 10 degrees. It is difficult to say if experimental measurements will lead to similar results, but it would be interesting to study it experimentally. Indeed, although the spatial electric field distribution can significantly be affected by the tip angle, it is very surprising that it plays such an important role in ionic wind velocity.

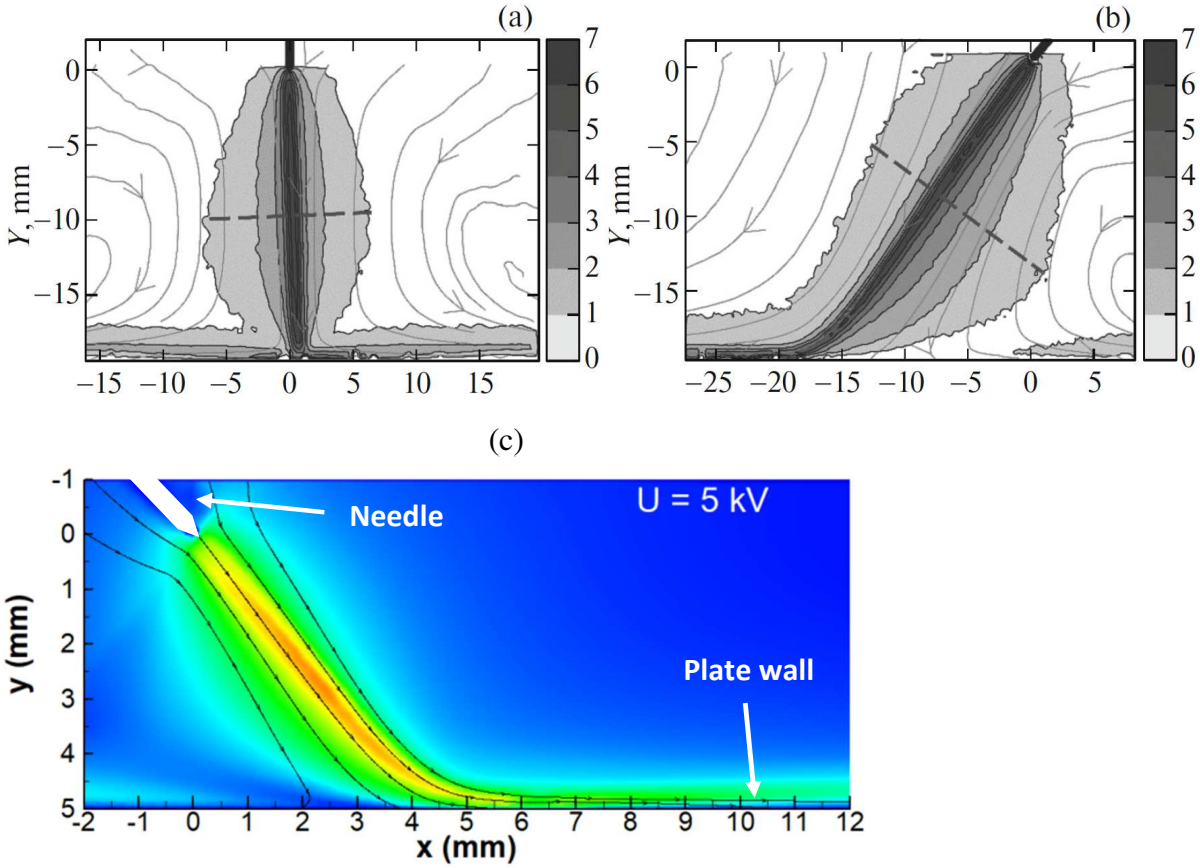

Fig. 15. Velocity fields of the ionic wind as a function of the needle angle: LDV measurements of Elagin et al. [93] (a, b) and PIV measurements of Moreau et al. [91]. In the two cases, the needle tip is located at x = 0 and y = 0.

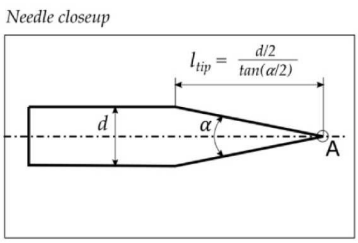

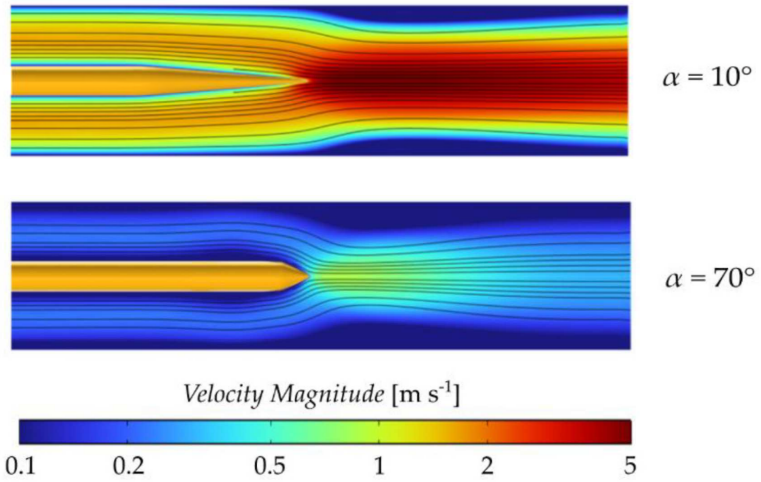

Fig. 16. Numerical simulation of the ionic wind for two different values of the tip angle [95].

Finally, let us say a few words about the environmental parameters. This description will not be exhaustive as the study of the effects of environmental parameters is not the focus of this article, but we cite some experimental studies on the subject. Concerning the effect of the pressure of the ambient air, Lee and Lau [96] showed that the ionic wind velocity decreases when the pressure is increased over atmospheric pressure, and they were able to measure a significant ionic wind even at 2.5 bar. Other authors measured the force produced by the discharge when the pressure drops [80,97]. They highlighted that at a constant ratio V/P (with V the voltage and P the pressure) or a constant discharge current I, the EHD force decreases roughly linearly when the pressure is decreased. This is mainly due to an increase in ion mobility at low pressure (see Equation 1). Concerning the effect of the relative humidity, Zhao showed that at a fixed voltage, the force lightly decreases when the humidity increases [97]. Zeng et al. [98], with a complex multi-electrode setup, demonstrated that the velocity decreases when the humidity increases at a constant voltage value because the discharge current is smaller at high relative humidity values. Furthermore, it has been highlighted by several authors that the temperature does not affect strongly the produced ionic wind [80,98].

3.4. Efficiency and enhanced corona discharges

Let us conclude this part with two points of information. The first one is that the efficiency of corona discharge in converting electrical power in mechanical power is very weak. The first author who computed this efficiency by dividing the discharge-induced mechanical power by the electrical power consumption was Robinson in 1961 [22]. In this wonderful and pioneer article, Robinson reports efficiencies between 0.2 and 1 %. This is very low, as most electrical energy is converted into heat. The temperature remains low, however, since the electrical power is low (a few hundred mW). However, the computation of Robinson was not precise because he had taken into account the average velocity to compute the mechanical power, whereas this velocity must be integrated in space. Therefore, in 2008, Moreau and Touchard proposed a more accurate method to compute the discharge efficiency [87]. In this study, among other things, the authors investigated the effect of several geometrical parameters on the discharge efficiency, and they found a maximum efficiency of 1.7 %. However, the method was also incomplete as the velocity was integrated in the x direction when it should also be integrated in the y direction (in the direction of the ionic wind jet). In fact, the best manner to correctly compute the mechanical power P_{mech} is to integrate the product of the force by the velocity over the discharge volume, such as in Giepman and Kotsonis [99] :

$$P_{mech} = \iint_S F_{EHD}\,(x,y) \times V_G(x,y)\,dxdy$$

where F_{EHD} and V_G are the time-averaged value of the EHD force and the ionic wind velocity. For that, we need to determine the velocity by PIV everywhere in a 2D plane and compute the force from the velocity information [100]. That is very complicated because to conduct this type

of computation with a needle-to-plate configuration, we must have a very high spatial resolution very close to the needle tip (in the order of 10 μm), where the force is the highest.

The second piece of information is that there are other ways of generating ionic wind. Of course, there are all the setups and configurations that the readers can find in the two previous review papers and that usually tinker with the electrode geometry [42,43]. However, for all these configurations, the ionization phenomenon is always due to applying a high voltage between at least two electrodes, an active high voltage one and a collecting one. In fact, there are also other ways to induce the ionization phenomenon. For instance, Orriere et al. used a nanosecond pulse micro-plasma to separate the ionization and drift phenomena [101], Park et al. used a pulsed plasma jet [102] and Du et al. [103] ionized the air with the help of a laser.

4. Ionic wind versus time

In this part, we aim to discuss the time-resolved properties of the ionic wind produced by corona discharges. To the best of our knowledge, on the one hand, only two research teams experimentally studied the dynamics of the ionic wind versus time (except one very recent article [92]), so this part will only be based on the articles of these two teams. This part is divided into several sections. First, we aim to characterize the ionic wind dynamics when DC positive and negative corona discharges are switched on. Second, we will present the effect of negative Trichel pulses and positive breakdown streamers on the ionic wind dynamics. Third, we will show that the temporal behavior of the ionic wind dynamics can be controlled when the corona discharge is powered by an AC high voltage.

4.1. Ionic wind dynamics when the discharge is switched on

The first series of experiments on the time-resolved behavior of ionic wind was carried out by the research team of Mizeraczyk from 2016 [54,104–106]. In the beginning, the authors of these articles wanted to observe the motion of smoke particles in an electrostatic precipitator

without necessarily knowing precisely if these particles moved under the effect of the ionic wind or under the effect of their own electrical charge in an electric field. Their experiments aimed at characterizing the transient electrohydrodynamic phenomena occurring on smoke particles suspended in quiescent air, when they are subject to a DC negative needle-to-plate corona discharge.

Fig. 17 presents some visualizations of the particle displacement when the negative high voltage is switched on. As the rising voltage front is slow, the discharge starts to ignite at t = 6 ms. The voltage and the current are respectively equal to - 8 kV and - 6 µA, and the electrode gap is fixed to 25 mm. At t = 6 ms, the EHD flow begins. At t = 40 ms, we can observe that the EHD flow progresses toward the plate, and it impacts it at around t = 100 ms. On the last visualizations (t = 240 ms), the flow is well-established and we can see two wide counter-rotating vortices on both sides of the location where the ionic wind impacts the plate. From these nice pictures, we can assume that the main phenomenon is ionic wind as what we can see at t = 106 and 240 ms is typical of a fluidic jet impacting a plate. If the particles were subject to Coulomb force (due to their own electric charge), the topology of the jet would follow the electric field lines, which is not the case. Moreover, these visualizations highlight very interesting features. First, when the ionic wind starts to flow from the needle tip, we can see a zone without any particles. Secondly, and it is more visible in Fig. 18, which presents a zoomed view of the jet front, the jet core is dark, suggesting that the particle concentration is low in it. On the contrary, the bright surface of the jet front, which shows a high concentration of particles, suggests that the jet front pushes the particles. In fact, the experiments show the "formation of a ball-like structure of the particle flow at the needle tip and its evolution into a mushroom-like object moving with an average velocity of about 2.5 m/s toward the collecting plate", as written is [54].

In a second article [104], the same authors explained the underlying physics, and they showed that the formation of two types of minijets (mushroom-like and V-like minijets) was linked to Trichel pulses and the cloud of negative ions that traverse the electrode gap when a Trichel pulse takes place, from the needle tip toward the collecting plate (Fig. 19). Finally, in 2018, they published a longer article in which they summarized all their results and they do the link between the discharge regime and the flow structure [106]. As an example, Fig. 20 presents a visualization of the flow with the velocity vector field, indicating that the velocity reaches about 2.5 m/s in front of the needle tip.

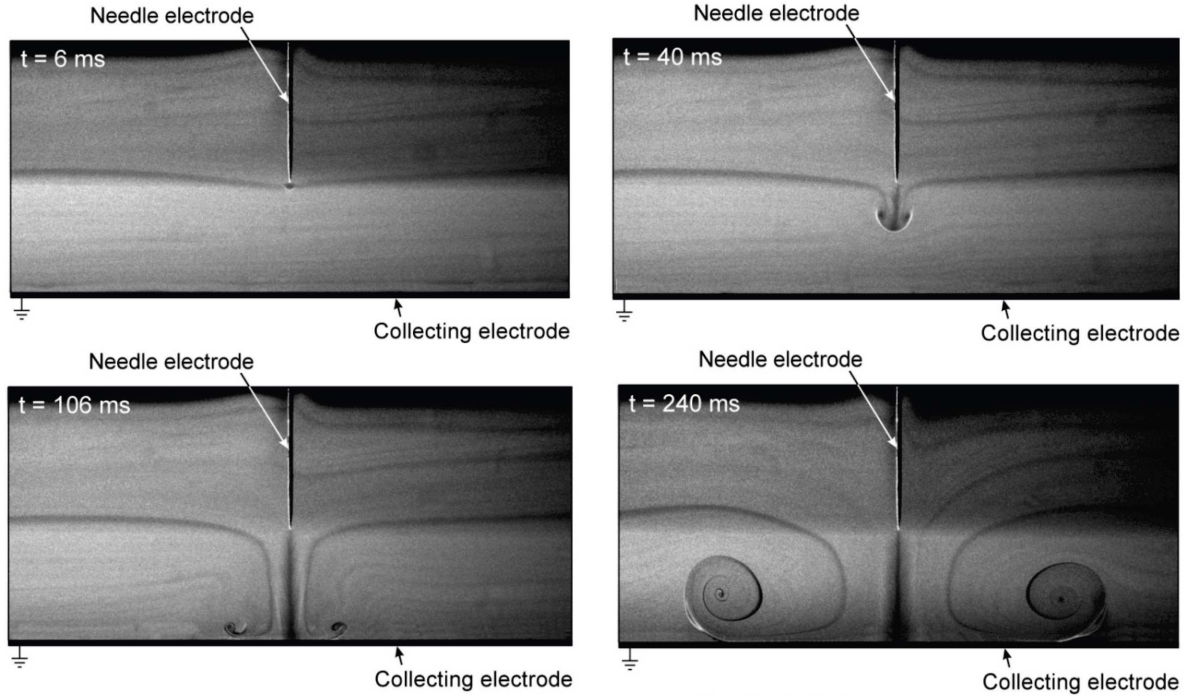

Fig. 17. Visualisations of the particle displacement when a DC negative needle-to-plate corona discharge is ignited. These visualisations come from Mizeraczyck et al [54] (the initial figure contains eight visualisations).

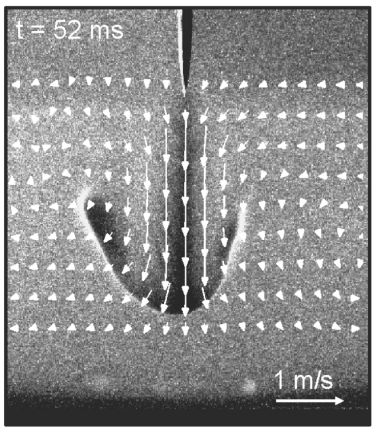

Fig. 18. Zoom view of the mushroom-like ionic wind jet [54].

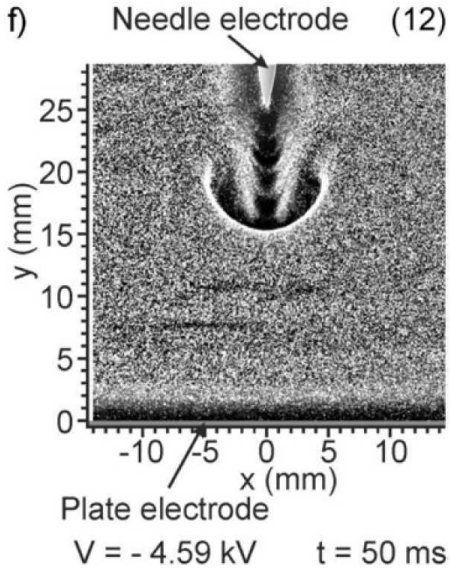

Fig. 19. Zoom view of the mushroom-like structure in front of the ionic wind jet, and the V-like minijets downstream of it [104].

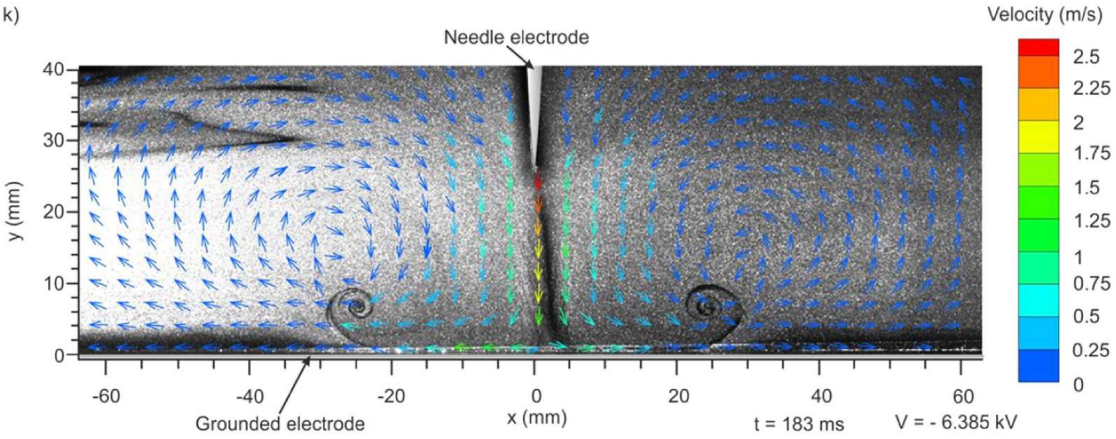

Fig. 20. Wide view of the ionic wind induced by a DC negative needle-to-plate corona discharge, and the velocity vectors of the ionic wind [106].

The same year, in 2018, Moreau et al. [67] confirmed the presence of this mushroom-like jet, with a zone without particles when the negative corona discharge is switched on (Fig. 21). More recently, this phenomenon has also been reported by Yang et al. [92]. The question then arises: is this phenomenon really due to the ionic wind, or could it be due to the charge of the particles close to the needle tip? To be honest, at that time, the answer was not easy, even if it seemed that this was due to ionic wind. To confirm this assumption, Fig. 22

presents Schlieren visualizations of the EHD flow induced by a negative corona discharge, at t = 0.5 ms and 2 ms after the discharge is switched on. The advantage of the Schlieren technique is that it does not require seeding particles. Therefore, what we see is either due to a gas flow or a thermal effect, but not on the potential charge of particles [51]. In these two visualisations, even if their quality is not very good, we can clearly see the mushroom like jet, which is induced from the needle tip and that progresses in the inter-electrode space.

To conclude, we can honestly think that the phenomenon observed by Mizeraczyck's team results from a strong EHD force due to Trichel pulses. This highlights that Trichel pulses (which correspond to a very fast phenomenon) are able to modify the ionic wind dynamics. However, this electrohydrodynamic phenomenon is not due to one single Trichel pulse only but to successive Trichel pulses occurring at high frequencies.

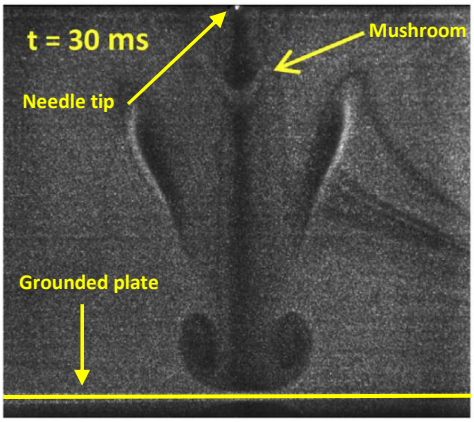

Fig. 21. Visualisation of the ionic wind produced by a negative needle-to-plate corona discharge. This picture come from [67].

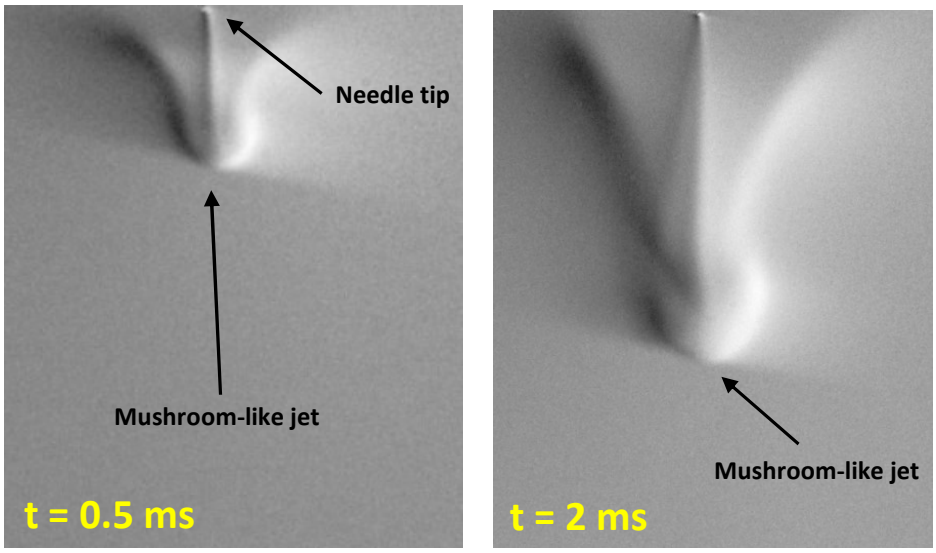

Fig. 21. Schlieren visualizations of the mushroom-like ionic wind jet when a negative corona discharge is switched on at t = 0 (not previously published).

The second series of experiments on the time-resolved behavior of ionic wind was carried out by Moreau et al. in 2018 [51,67,75,76,88]. In their experiments, the authors studied the dynamics of ionic wind on DC positive and negative needle-to-plate corona discharges and AC corona discharges. Some results are presented in this article. For instance, Fig. 22 shows three examples of the instantaneous velocity fields at t = 1, 2, and 4 milliseconds after the discharge is switched on, for a DC positive corona (on the left) and a negative one (on the right). The gap equals 25 mm, and the applied voltages are ±16 kV (reached in 32 µs after the high voltage is switched on at t = 0 as the slew rate of the TREK amplifier used in this study equals 500V/µs). In the case of a positive corona, a thin ionic wind jet starts from the needle tip with a maximum velocity of around 5 m/s, 1 millisecond after the discharge ignition. Then, the jet progresses toward the plate and reaches it in 6.7 milliseconds (not visible here). When the ionic wind jet impacts the plate, two counter vortices are formed, such as in Fig. 20. The jet topology is cone-shaped, and the velocity at the middle of the jet varies from about 7 m/s up to 10 m/s, as it is not constant between the needle tip and the jet front. Moreover, the front of the jet seems to be very unsteady.

In the case of a negative corona discharge, the jet is slower as it needs 10 milliseconds to reach the plate. The velocity along the jet, in front of the needle tip, is more constant (around 5 m/s) than the positive jet. This confirms previous results: the negative jet is slower and more stable than the positive one.

Fig. 23 presents another example of results concerning the positive corona discharge [51]. On the left, one can see the velocity vectors of the ionic wind at the same moments as in Figure 22 (t = 1, 2, and 4 ms). On the right, Schlieren visualizations are presented at the same time. First, let us comment on the velocity vector fields. As we can observe, the jet seems unsteady, with structures developing at its front. As it expands, it seems to fluctuate like a pulsed blowing jet (clearly visible at t = 4 ms). Moreover, at t = 2 ms, we can see two separated zones: a first one with a cone-shaped (between $0 \leq x \leq 7$ mm) and a second one corresponding to the jet front ($8 \leq x \leq 12$ mm). At the front of the jet, the velocity is higher, highlighting the presence of a strong EHD force, certainly due to the space charge left after the propagation of an intense and arborescent breakdown streamer during the rising voltage front (see the original articles for more details).

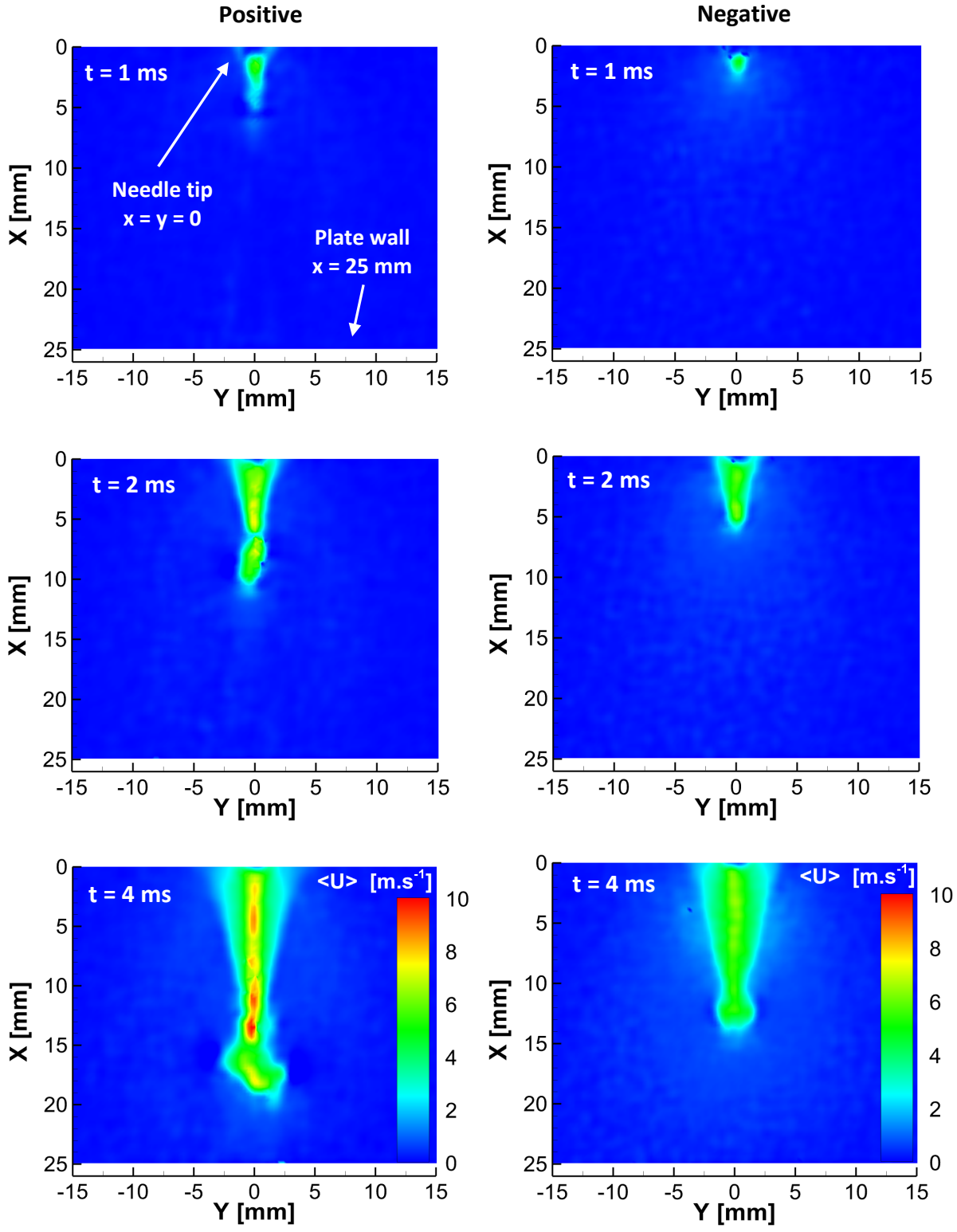

Fig. 22. Instantaneous velocity fields at t = 1, 2 and 4 milliseconds after the discharge is switched on, for a DC positive corona (on the left) and a negative one (on the right). The gap is equal to 25 mm and the applied voltages are ±16 kV. The needle tip is located at x = 0 and y = 0. The plate is located at y = 25 mm.

Let us now comment on the Schlieren visualizations and why the authors conducted such visualizations. The reason is simple: the authors wanted to cancel any suspicion of seeding particle charge as in this case, what they observed with a PIV system could be due to the Coulomb force acting on these particles instead of the ionic wind. In fact, they wanted to ensure that the moving particles correctly followed the trajectory and the dynamics of the ionic wind. The first important information is that the Schlieren method allows for correct visualization of the ionic wind. Indeed, although Schlieren imaging leads to qualitative information, we can see that it matches those obtained with the PIV measurements, thereby demonstrating that the motion of the particles (when these are correctly chosen, which is the case here) is due to ionic wind. Secondly, the Schlieren visualizations highlight that the front of the ionic wind jet is fully perturbated as it is the seat of a highly unstable EHD force.

4.2 Temporal behavior of the ionic wind

After investigating the transient state of the ionic wind when the discharge is switched on, Moreau et al. [51] studied the time-resolved behavior of the ionic wind when it is well-established, a long time after the discharge ignition. Let us first consider the case of the positive corona discharge. Indeed, as the ionic wind seems to be very unstable, as a pulsed jet (see the vector field of Fig. 23, at t = 4 ms), the authors wanted to know if only the jet front was unstable or if the ionic wind jet was unstable too, even a long time after the discharge ignition. Moreover, they wanted to know if some frequencies could be identified in the ionic wind dynamics. For that, the power spectra density (PSD) of the ionic wind velocity was computed at different x locations in front of the needle tip for different positive voltage values, both in the glow regime and the breakdown streamer one. The results were a great surprise. On the one hand, there was no peak in the PSD in the case of the glow regime. On the other hand, in the case of the breakdown streamer regime, the authors observed a big PSD peak,

the frequency of this peak corresponding exactly to the streamer frequency computed from the current versus time curves i(t), such as in Fig. 3c. This result was important as it demonstrated for the first time that the EHD flow dynamics was fully affected by the streamer occurrence. It was concluded that the jet instability was certainly due to a strong positive space charge left after the propagation of every breakdown streamer.

This feature is confirmed by Fig. 24, which presents an instantaneous Schlieren visualization of the well-established ionic wind produced by a positive discharge (the voltage equals + 16 kV, and the electrode gap is 25 mm). Indeed, it highlights the strong instabilities of the jet produced by a positive breakdown streamer discharge. It seems that the jet is disturbed every time a breakdown streamer occurs. To estimate the frequency of these instabilities, we can approximatively determine the distance between two successive instabilities in Fig. 24 (around 2 mm) and divide this length by the ionic wind velocity (around 8 m/s, see Fig. 8), then we have the time Δt between two successive instabilities. Thus, the instability frequency is equal to $1/\Delta t$, *i.e.* about 4 kHz. This value perfectly corresponds to the breakdown streamer frequency in these conditions [51].

In the case of a negative corona discharge, the jet is much less unstable [61,67]. To illustrate this assumption, Fig. 25 presents a map of the velocity fluctuations (root mean square values) for the two polarities, at ± 16 kV. For the positive discharge, we can see important velocity fluctuations as the rms velocity reaches 10 % of the time-averaged velocity (for this voltage value, the positive discharge regime is the breakdown streamer one). On the contrary, with the negative discharge, the fluctuations are very weak, highlighting a constant velocity and then a stable ionic jet. Furthermore, the authors of this article showed that the map of velocity fluctuations at +12 kV looked like the one observed at - 16 kV, highlighting that the positive ionic wind is stable when the discharge is glow.

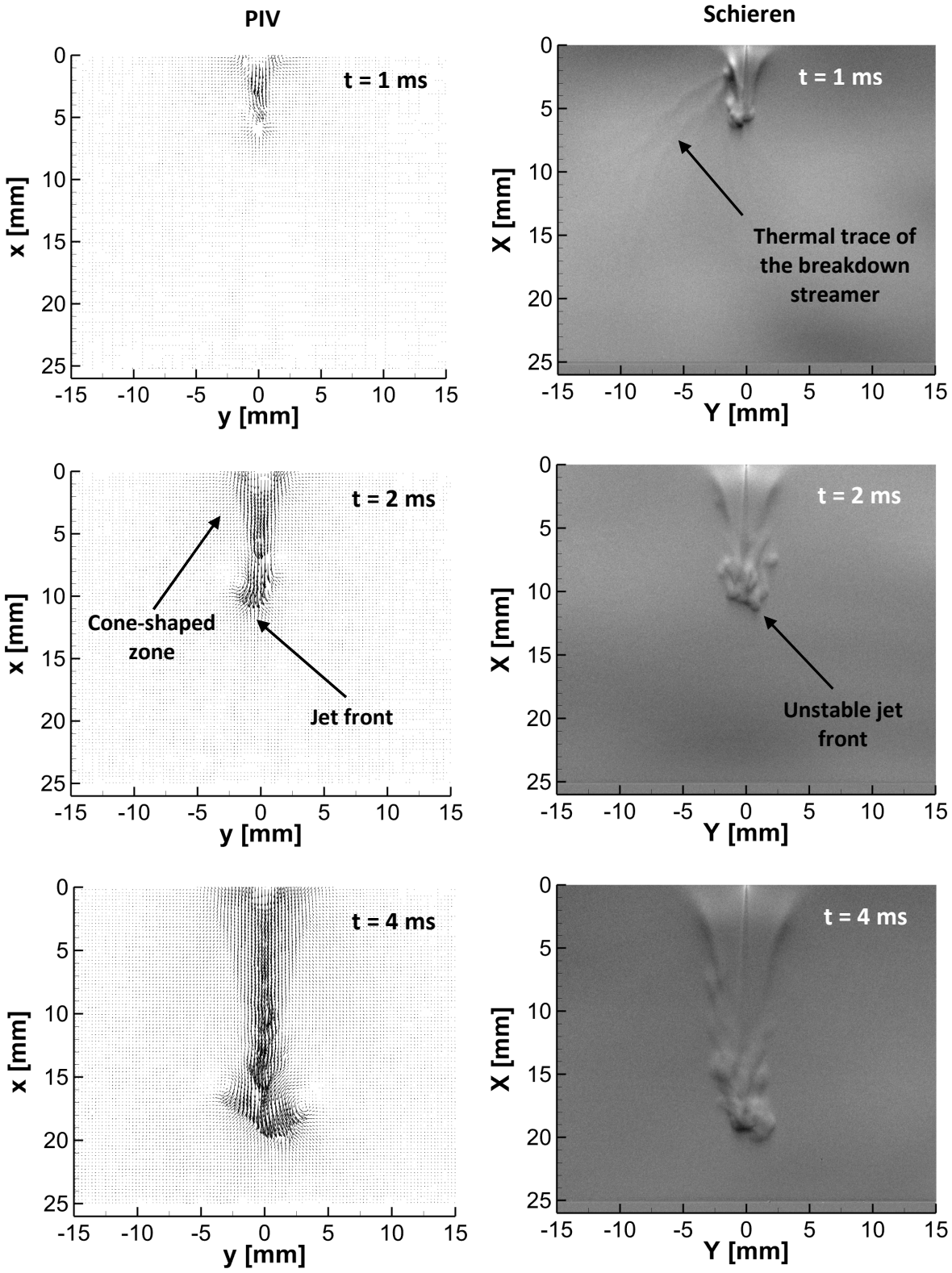

Fig. 23. Instantaneous velocity fields (on the left) and instantaneous Schlieren visualizations (on the right) at t = 1, 2, and 4 milliseconds after the discharge is switched on, in the case of a DC positive corona discharge. The gap is equal to 25 mm and the applied voltages are ±16 kV. The needle tip is located at x = 0 and y = 0. The plate is located at y = 25 mm. Figures from [51].

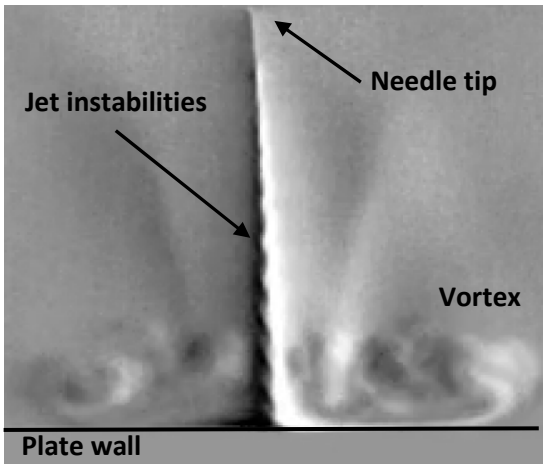

Fig. 24. Instantaneous Schlieren visualizations of the ionic wind jet produced by a positive corona discharge (not previously published).

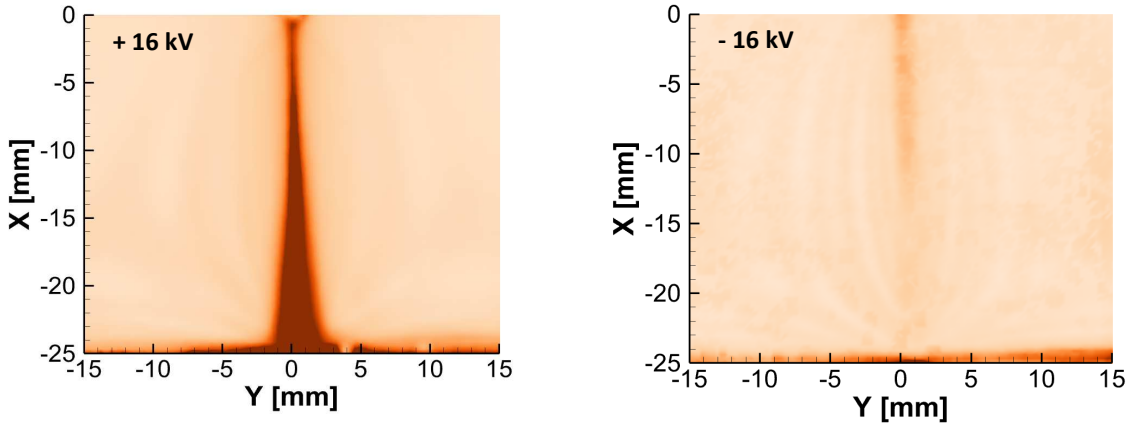

Fig. 25. RMS velocity fields of the ionic wind at + 16 kV (left) and - 16 kV (right). Data from [67]

To finalize this section on the time-resolved velocity of ionic wind, let us comment on the results obtained with an AC needle-to-plate dielectric barrier corona discharge [75,76]. Only one example is shown in the present article but readers can consult the original articles for more details. Fig. 26 presents the x component of the instantaneous ionic wind velocity Ux versus time in front of the needle tip for four different high-voltage waveforms (V_{AC} = 14 kV, f_{AC} = 50 Hz). Two different features were observed. On the one hand, for the sine, triangle, and sawtooth waveforms, there is a flow acceleration during both the positive and the negative half-cycles of the applied voltage, the positive discharge being more effective in

velocity production. That confirms all the previous results: the positive corona discharge induces a faster ionic wind than the negative one. On the other hand, for the square waveform, the increase in velocity occurs during the rises and falls of the voltage, because of the strengthening of the electric field due to the ions remaining from the previous half-cycle at the wall of the dielectric barrier.

Furthermore, the authors highlighted a frequency effect. Indeed, up to about 500 Hz, there are always two velocity bumps per high voltage period (one during the positive half-cycle and another one during the negative half-cycle). Between 500 Hz and 1 kHz, the positive ionic wind takes over the negative one and the velocity peak due to the negative discharge was very weak. From 2 kHz, there is only one single flow acceleration per voltage cycle, as the ionic wind produced by the positive corona discharge totally takes over the ionic wind produced by the negative corona because it is more intense and faster.

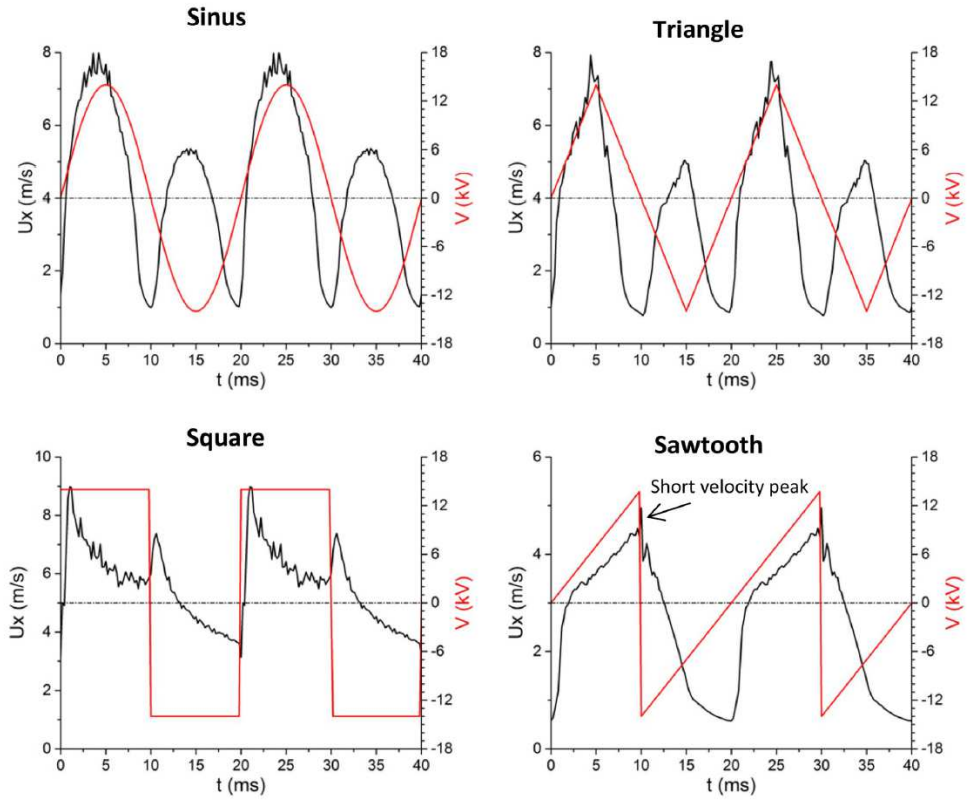

Fig. 26. X component of the ionic wind velocity Ux versus time, in front of the needle tip, for four different high voltage waveforms (V_{AC} = 14 kV, f_{AC} = 50 Hz) [76].

5. Modelling and numerical simulations of ionic wind

In this part, the goal is not to draw a thorough overview of the numerical simulations on the corona discharge physics and ionic wind. Here, we just aim to explain the behaviors observed experimentally in the third and fourth parts, with the help of modeling and a few numerical simulations of the ionic wind phenomenon. We aim to explain why the two jets produced by positive and negative discharges differ. In the first part, we will explain why the time-averaged ionic wind jet produced by a negative discharge is wider and slower. Second, we will discuss the role of breakdown streamers and Trichel pulses on the ionic wind, specifically on its temporal behavior.

5.1. Time-averaged ionic wind

Several authors contributed to describing the ionic wind phenomenon by numerical simulations [107,53,108,109,90,110], and some of them searched to explain the difference between the positive and the negative ionic winds. First, we do not start with a numerical simulation but with the photos of Ferreira et al [111], in the case of a needle-to-plate corona discharge (Fig. 27). These pictures, taken with a simple digital camera (exposure time = 15 seconds), clearly show that the region that emits light, where the discharge is active, is wider and more extended in the case of the negative discharge. Moreover, they highlight that the positive discharge, in the glow regime, is confined very close and in front of the needle tip.

In a recent publication, Bouzza et al [107] compared positive and negative corona discharges with the help of numerical simulations of the ionic wind produced between a wire and a plate. Assuming that the region where the electron density is the highest corresponds to the active region of the corona discharge, their results confirmed the photos of Fig. 27. Indeed, Fig. 28 presents the spatial distribution of electrons in the case of a positive discharge (V = + 9 kV, I = 47 µA) and a negative one (V = - 9 kV, I = - 59 µA). One more time, we can see

that the negative corona discharge has a larger extent. Indeed, in the case of a positive discharge, positive ions are generated by ionization very close to the wire wall (in the ionization region) and then drift toward the grounded electrode under the effect of the electric field. Thus, the space charge between the two electrodes is positive, and the EHD force is always directed toward the plate. On the contrary, in the case of a negative corona discharge, the maximum electron density is not around the wire wall but at a distance of about 300 µm from the wire wall. Therefore, the spatial distribution of electrons is larger (Fig. 28, on the right). Then, positive ions produced by ionization drift toward the wire, whereas negative ions formed by electron attachment drift toward the plate. This results in a positive space charge in the ionization region and a negative space charge in the drift region.

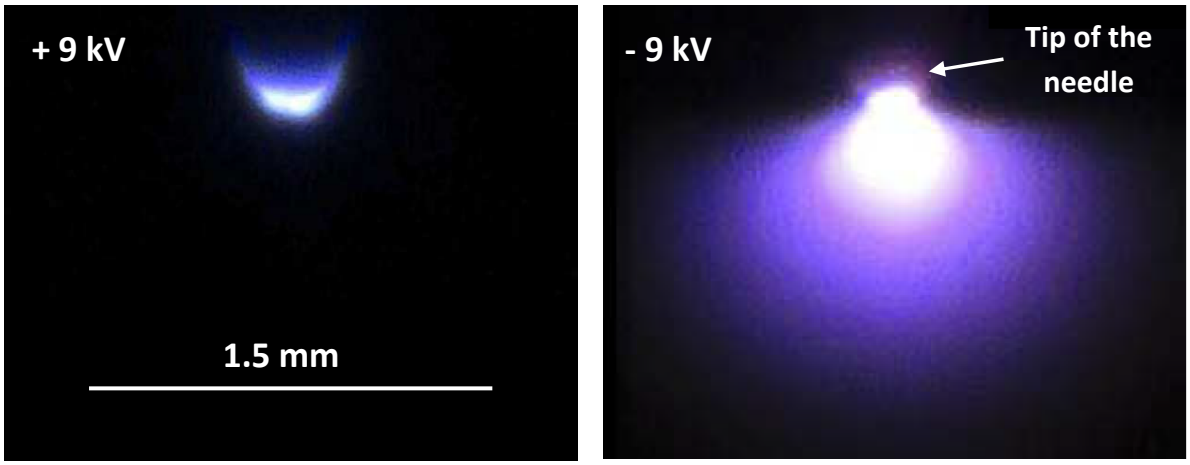

(a) (b)

Fig. 27. Photos of positive (a) and negative (b) needle-to-plate corona discharges. The gap is 14 mm, and the applied voltage equals 9 kV. Exposure time of 15 seconds. Photos from [111].

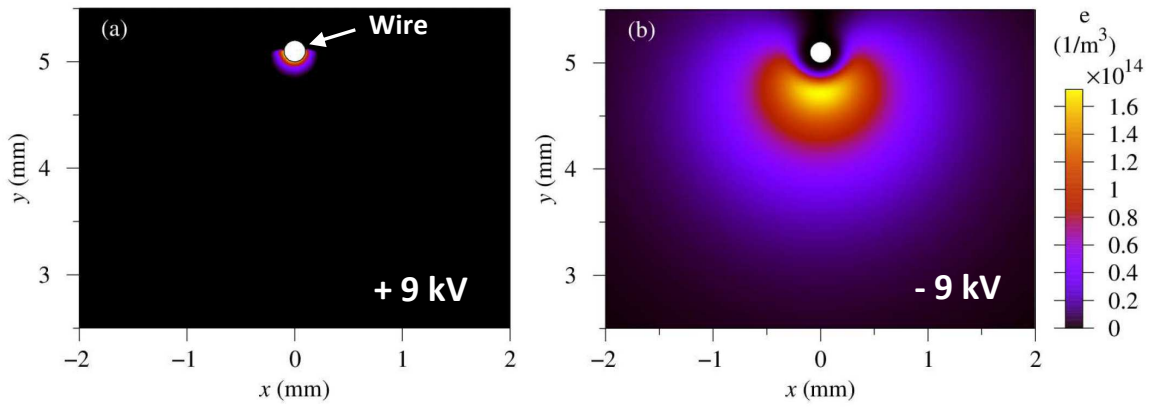

Fig. 28. 2D spatial distribution of electrons around the wire electrode for + 9 kV (a) and – 9 kV (b) [107].

This feature had already been highlighted by several authors [53,109,110] and recently confirmed by Asipuela and Ivancsy [108]. Fig. 29, which presents numerical simulations of Mantach and Adamiak [53], shows the distribution of electrons, positive ions, and negative ions in the case of a negative needle-to-plate corona discharge. First, we can clearly see that there is a positive ion cloud in the ionization region, and as for Bouazza et al, this region is limited to a distance of around 300 µm from the needle tip. Secondly, the width of this region is very small (about 200 µm). Third, the density values are very different as they are in the order of 10^{16}, $10^{17,}$ and 10^{18} m^{-3} for electrons, negative ions, and positive ions, respectively. As a result, the authors showed that this high concentration of positive ions results in a strong counter-EHD force in the direction of the needle tip in the ionization zone. Concerning the negative ions, there are none in the ionization zone, but their density suddenly increases when one moves away and leaves this zone. Thus, because of mutual repulsion between negative ions, they drift in the radial direction (in the width direction), leading to a decrease in their concentration and a wider zone containing negative ions (up to about 1 mm). This can explain why the negative ionic wind is wider than the positive one. From similar numerical simulations, Chen et al [110] assume that the positive EHD force in the ionization region can reach 1.22×10^8

N/m^3 when the negative force occurring in the drift region is 1-2 orders of magnitude smaller but covers a larger area.

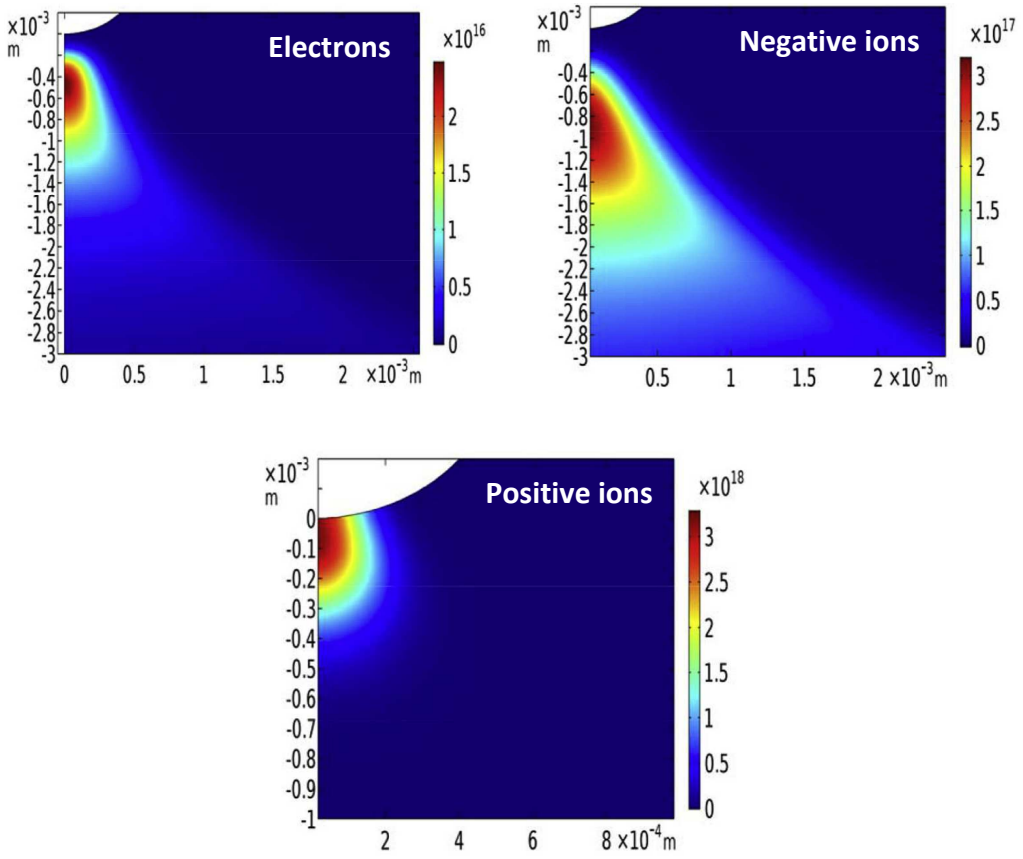

Fig. 29. Example of 2D density spatial distribution of electrons, negative ions and positive ions in the case of a negative corona discharge with a voltage of -12 kV. Pictures from [53].

To finish comparing positive and negative corona discharges, Fig. 30 presents the density of electrons, positive ions, and negative ions between a wire and a plate, r = 0 corresponding to the high voltage wire wall [108]. The gap equals 65 mm, the applied voltage equals 20 kV, and the discharge is uniform and diffuse; Trichel pulses and breakdown streamers are not considered in this model. On the one hand, for the negative discharge (Fig. 30a), it is one more time demonstrated that positive ions are more numerous and close to the active electrode (in the ionization region), as it had already been demonstrated by Chen and

Davidson more than twenty years ago [112]. In Fig. 30a, for r < 0.1 cm, the density of positive ions reaches 10^{15} m^{-3}. From r = 0.1 cm, the density of negative ions becomes higher than the one of positive ions and is also equal to about 10^{15} m^{-3}. On the other hand, in the case of a positive discharge, the positive ion density is the highest throughout the inter-electrode space, and it is constant in the drift region, at least up to 2 mm (Fig. 30b). This does not mean that the EHD force is constant in the drift region as it is equal to the product of the space charge and the electric field, the electric field decreasing when one moves away from the needle tip. Moreover, its value (less than 10^{14} m^{-3}) is weaker than the negative ion density for the negative discharge (around 10^{15} m^{-3}). Although we cannot be sure of the density values, and although it is difficult to compare the different numerical simulations since the input parameters are never the same, the curves of Fig. 30 show a trend that confirms the results presented above, and the numerical simulations of Liu and Becerra in 2016 and 2017 [109,113].

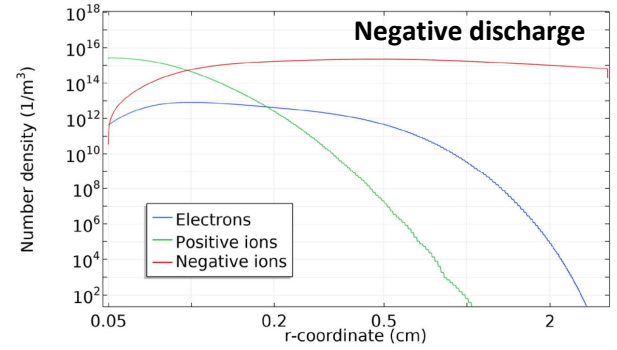

(a)

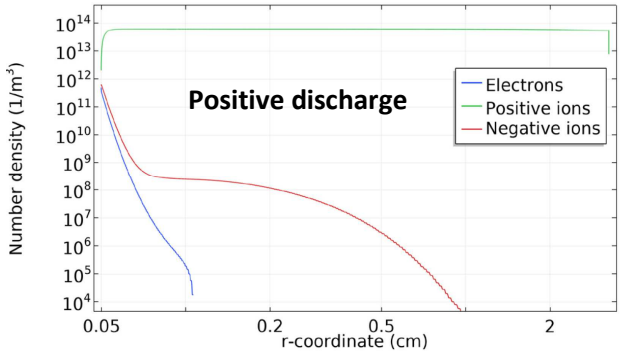

(b)

Fig. 30. Density of electrons, positive ions, and negative ions between the two electrodes for negative (a) and positive (b) corona discharges, r = 0 corresponding to the high voltage electrode wall [108].

To summarize, it is clear that all these studies lead to a consensus, and they explain what has been observed experimentally and what has been presented in the third part. In the case of a positive corona discharge, the positive space charge is confined in front of the needle tip (or wire) and does not extend in the width direction. Moreover, the space charge is positive throughout the inter-electrode space, resulting in an EHD force always oriented from the active electrode toward the grounded one. This results in a fast and pointed ionic wind jet, especially when the regime is the breakdown streamer. On the contrary, for the negative corona discharge, the ionization region is positive, resulting in an EHD force toward the active electrode and thus, a very fast flow toward it [53,68]. Then, this counter-EHD force in the ionization region results in a decrease in the ionic wind, even outside of the ionization region, as what happens very close to the tip affects the whole ionic wind. In the drift region, the negative space charge extends over a larger width (see Fig. 29), resulting in a wider ionic wind jet. Furthermore, if we look at the results of Fig. 7 in detail for voltages equal to ± 10 and ± 12 kV, the presence of the positive space charge (and then a counter-positive EHD force toward the active electrode) in the ionization region of the negative corona explains why the ionic wind velocity produced by the negative discharge in the first millimeters ($x < 5$ mm) is always smaller than the one produced by the positive discharge.

5.2. Influence of Trichel pulses and breakdown streamers on the ionic wind dynamics

In this section, we discuss the role of the Trichel pulses and the breakdown streamers in the dynamics of the ionic wind. However, there are only a few studies, so it will not be easy to conclude.

Concerning the negative corona discharge, several authors computed the ion density close to the active electrode during one single Trichel pulse, from the pulse initiation until its end, the typical Trichel pulse duration being a few hundred nanoseconds [110,114,90,115]. However,

to our knowledge, only Chen et al [110] investigated the effect of the Trichel pulses on the ionic wind dynamics. For example, Fig. 31 presents the density of negative ions, electrons, and positive ions at four different time steps [115]. At step 1, positive ions are produced very close to the needle tip, in the ionization zone, and negative ions and electrons outside this zone, as in Fig. 29. At step 2, which corresponds to the current peak phase, the densities of negative ions, positive ions, and electrons are maximum. Then, from step 3 and step 4, we can see that the negative ion cloud moves toward the plate. However, we do here a very simple description of the numerous physical phenomena occurring during one single Trichel pulse and readers are advised to read the original articles for a fuller description, especially the one of Chen et al. [110]. Indeed, the authors investigated in detail the EHD force and the resulting ionic wind velocity during one single Trichel pulse and between two successive pulses. Moreover, they clearly explained the physical phenomena near the active electrode during and after one single Trichel pulse. They showed that the unsteady phenomenon was complicated because it varied in time and space. To sum up, they highlighted that the total body force between the two electrodes decreases during the Trichel pulse because the positive EHD force (due to the high density of positive ions in the ionization region) increases more than the negative EHD force due to the motion of negative ions in the drift region. Consequently, the velocity close to the needle tip is pulsed (at a distance equal to 100 µm from the tip wall) because it decreases during every Trichel pulse (see point P in Fig. 32). However, this feature is no longer visible when one moves away from the needle as at a distance of 0.5 mm from the needle tip, the velocity is no longer pulsed (point Q Fig. 32). To conclude, from a macroscopic point of view, these numerical simulations of Chen et al highlight that that the Trichel pulses do not play a significant role on the topology and the velocity of ionic wind because their effect is limited to the ionization region.

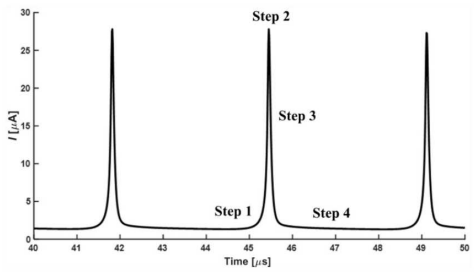

(a)

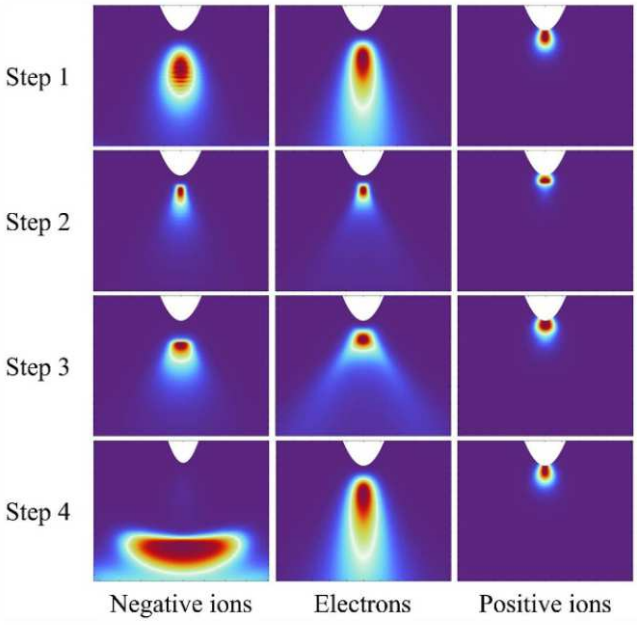

(b)

Fig. 31. Discharge current versus time with the different steps of a Trichel pulse (a), and densities of negative ions, electrons and positive ions at these four steps (b). Data reproduced from [115]. The density scale is not indicated in the initial article.

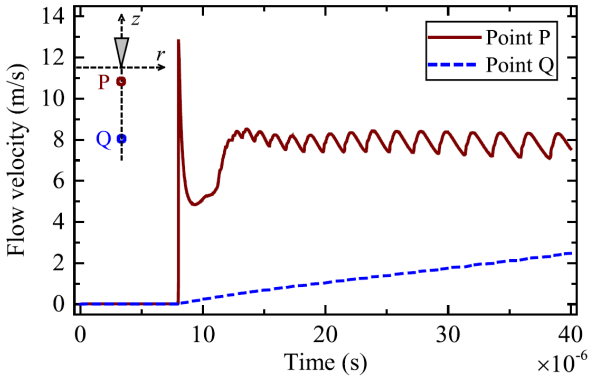

Fig. 32. Ionic wind velocity produced by a negative corona discharge when the high voltage is switched on, for two different locations: the point P is located at 100 µm far from the needle tip and the point Q is at 0.5 mm. Figure from [110].

Concerning the positive corona discharge, the experimental results of the fourth part showed us that the breakdown streamers play a key role in the ionic wind as (1) the velocity increases suddenly when the discharge regime transitions from the glow regime to the breakdown streamer one, (2) the ionic wind is pulsed at the same frequency than that of the streamers. To the best of our knowledge, only two articles deal with the effect of streamers on the ionic wind by numerical simulation.

In 2002, Loiseau et al [116] conducted numerical simulations of the ionic wind produced by one single breakdown streamer. The discharge is ignited between a needle and a plate spaced by 10 mm. In this article, the authors presented several results. Still, we focus here on the evolution of the axial gas velocity in front of the needle tip during the propagation of one single streamer. Figure 33a shows the axial gas velocity at three moments: A (which corresponds to the discharge inception), B (30 ns after the discharge inception), and C (50 ns after the discharge inception). At t = 0, the streamer starts propagating, and its head seems to be located at about 0.3 mm from the needle tip. Then, the strong space charge of its head results in an EHD force and a gas acceleration, with a velocity of 0.35 m/s. At t = 30 ns, the breakdown streamer has reached half the distance between the two electrodes, and the gas velocity induced by the space charge of its head is still about 0.35 m/s. Behind the streamer head, the gas flow is due to some remaining positive ions after the progression of the streamer head. At t = 50 ns, the streamer impacts the plate. Finally, after the streamer propagation (during 100 µs), the authors showed that many remaining positive ions drift toward the plate. We can then consider that these ions contribute more to ionic wind than the streamer itself because the streamer propagation is very fast.

These results of Loiseau et al are very interesting but not intuitive from a mechanical point of view. The phenomenon described here has not to be considered like a fluid jet, like the ones

depicted in Fig. 22 and 23, so we have deliberately used the term gas flow and not ionic wind. Indeed, if the jet reached the plate in 50 ns, that would mean that the front of the ionic wind jet moves at a velocity that is not equal to 0.35 m/s but to 2×10^5 m/s (10 mm divided by 50 ns), which is not possible. This velocity corresponds to a local velocity. Loiseau et al determined the force exerted by the streamer head on the gas and computed the flow resulting from this EHD force. Then, when the streamer propagates at a velocity of 2×10^5 m/s and arrives at a given position, the gas at this position is driven to flow with a velocity of 0.35 m/s. However, we have to be honest: we cannot give a definitive answer about the validity of these results because it is impossible to verify them experimentally.

More recently, Chen et al. [68] investigated the effect of streamers on the dynamics of the ionic wind. Since a breakdown streamer is very difficult to simulate, the authors used an "artificial" streamer and computed the EHD force generated by this artificial streamer versus time. First, they estimated the EHD force exerted by the streamer head on the gas and plotted the velocity versus time during the first 100 nanoseconds. Their results were very similar to those of Loiseau et al, but the gas velocity induced by the streamer head was smaller (0.034 m/s). Secondly, Chen et al computed the time-evolution of the ionic wind during a few milliseconds. The authors considered that the discharge current was only due to breakdown streamers. They did not compute the EHD force due to the DC component of the discharge current, as they wanted to isolate and observe the contribution of the streamers only. The result is presented in Fig. 33b for three points (at 1, 10, and 20 mm far from the needle tip) and a streamer frequency of 3.7 kHz. This result is very interesting as it highlights that even far from the tip, the velocity is pulsed at 3.7 kHz; it increases when a breakdown streamer occurs and decreases between two successive streamers since no EHD force is exerted on the gas.

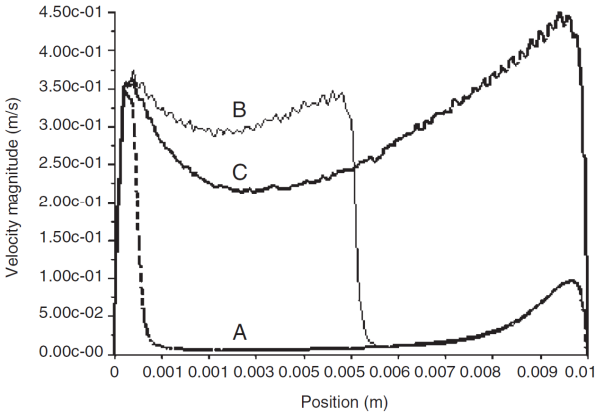

(a)

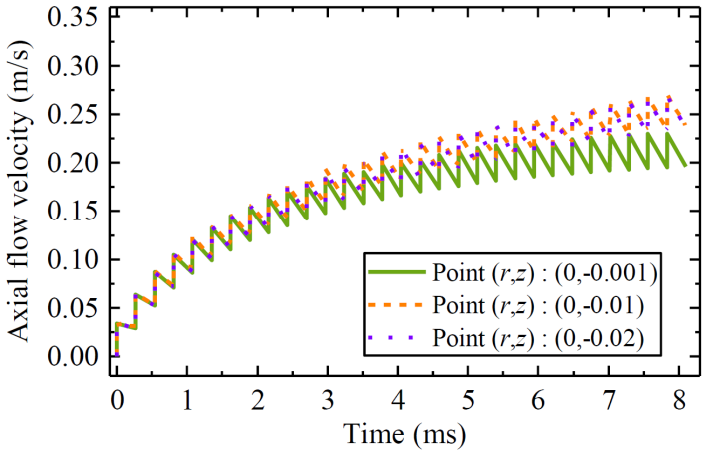

(b)

Fig. 33. Velocity of the ionic wind induced by one single breakdown streamer in front of the needle tip (a) and velocity versus time at three positions in front of the needle tip (b). Figures from [68].

To conclude this part, one can say that the numerical simulations of the time-averaged ionic wind clearly explain why the positive discharge produced a thin and pointed jet and why the negative discharge resulted in a wider and slower jet. Numerical simulation is a perfect tool for understanding the physics of the origin of the ionic wind. Concerning the numerical simulations of the Trichel pulses, we can trust their conclusions since different authors found very similar results. These results have shown that a strong counter-EHD force occurs in the ionization zone during one single pulse. Still, as this force is limited in time and space, it does not significantly affect the ionic wind outside the ionization region. Consequently, we can

regret that these numerical simulations do not allow us to explain the experimental observations of Mizeraczyk et al. [54] (Fig. 18 and 19). On the contrary, the simulations of Chen et al. clearly illustrate the role of the breakdown streamers. They highlight that the produced ionic wind is pulsed at the streamer frequency, as experimentally demonstrated by Moreau et al. [51]. However, the authors did not model and simulate the physics of breakdown streamers as they used an artificial streamer.

These comments, when negative, do not call into question the quality of the work of the researchers who carried out these numerical simulations. Indeed, it is well-known that it is very complicated to simulate the temporal behavior of ionic wind for two main reasons. First, the time scales of plasma physics and fluid mechanics are very different. When one wants to simulate a breakdown streamer or a Trichel pulse, the order of magnitude of the time step is the nanosecond. In contrast, the characteristic timescale in fluid mechanics is on the order of one millisecond. In our case, if we want to observe the influence of several breakdown streamers on the ionic wind, as their frequency is a few kHz, the simulation time must be in the order of at least one millisecond. Consequently, the computation time to simulate one millisecond of flow with a time step of one nanosecond is very high. Secondly, numerical corona discharge simulation requires very small grid sizes, especially near the needle tip. One more time, this is time-consuming. Finally, in most cases, these simulations use a model composed of only three species (electrons, positive ions, and negative ions) or, at best, a few chemical reactions, but their number is limited. However, if we want to run simulations that are faithful to reality, we should take into account a large number of chemical reactions taking place inside the discharge. Then the different positive and negative ions that are produced, and this would be even more prohibitive because of the computation time. Unfortunately, we are unlikely to see simulations capable of correctly simulating the physics

of the discharge, as well as the behavior of the ionic wind on the time scale of the breakdown streamers and the Trichel pulse. However, it is not the fault of those working on it; it is the fact that computing power is still too limited.

6. Conclusion

In this article, we have exclusively focussed on the physical phenomenon of the ionic wind.

We could have talked about the different techniques for measuring ionic wind velocity. We could have discussed the many applications of ionic wind, its prospects, and potential future applications. We did not do this because, as we said before, the aim was to describe the physical phenomenon as accurately as possible, based on current knowledge. The article is certainly imperfect, and it certainly lacks detail. However, the time available to write it was limited, and at some point, you had to hand in our copy, even if we felt something was still missing. Having said that, we did remind you of quite a few things about these corona discharges and the ionic wind they produce.

First, we discussed the electrical properties of corona discharges. We have seen that Townsend's equation can always correctly interpolate the experimental I-V characteristics of a negative corona discharge. On the contrary, in the case of a positive corona discharge, the measured current suddenly increases when the positive corona transitions from the glow regime to the breakdown one and is higher than the values predicted by Townsend's law. Second, we described the different discharge regimes. For the negative corona discharge, the regime most often observed is the Trichel regime, characterized by current pulses of several hundred kHz and a discharge confined around the needle tip. Two main regimes are observed

for the positive discharge: the glow one and the breakdown streamer one. These two regimes are very different as in the first case, the current is pulseless and the discharge is confined in the ionization region just in front of the needle tip. In the second regime, breakdown streamers cross the inter-electrode gap, leading to current pulses of a few mA at a few kHz. Despite this, the electrical power consumed by corona discharges is a few hundred mW, and its efficiency in electro-mechanical conversion is around 1%, which is very low. Third, we reminded that at a given voltage value, the mean current of negative discharges is, in most cases, higher than that of positive discharges. The reason for this is not necessarily very clear. The most plausible explanation seems to be that the current of a positive corona discharge is mainly due to the positive ions that move toward the plate inside the drift region. In contrast, the negative current is due to the drift of negative ions and electrons, which have a higher mobility. Moreover, the density of negative ions in the drift region of a negative corona discharge is higher than that of positive ions in a positive corona discharge (Fig. 30). That is certainly why the negative current is, in most cases, higher than the positive one. Finally, we have seen that when a corona discharge is powered by an AC voltage, a positive corona discharge occurs during the positive half-cycle, and a negative discharge occurs during the negative half-cycle, with the same properties as the DC corona discharges.

Afterward, in the third part, we described in detail the time-averaged characteristics of the ionic wind. First, we have seen that the ionic wind velocity increases approximately linearly with the voltage and the square root of the current. Secondly, when the discharge is ignited between a needle and a plate, the ionic wind consists of an air jet flowing from the needle tip toward the plate. In practice, the jet is 3D cone-shaped, and it should be, in theory, axisymmetric with respect to a straight line that goes from the tip towards the plate and

perpendicular to the plate. However, the jet is often not completely perpendicular to the plate, as the jet is not always stable.

In the case of a positive corona discharge, the positive space charge is confined in front of the needle tip and does not extend in the width direction. Moreover, the space charge is positive throughout the inter-electrode space, resulting in an EHD force always oriented from the active electrode toward the grounded one. This results in a fast and thin ionic wind jet. On the contrary, for the negative corona discharge, the ionization region is positive, resulting a EHD force toward the active electrode. In the drift region, the space charge is negative and extends over a larger width, leading to a wider ionic wind jet. However, the counter-EHD force close to the needle tip (size of about 300 µm) usually results in a slower negative ionic wind velocity, except at very low voltages for which the negative ionic wind can be faster than the positive one. After that, we have highlighted the key role of breakdown streamers on the ionic wind, as breakdown streamers lead to a significant increase in the time-averaged ionic wind velocity. Indeed, in the presence of streamers, the jet is faster and more pointed in front of the needle tip.

Finally, we have brought to light two interesting features. First, when the angle of the needle compared to the plate is modified, the ionic wind jet has the same angle as the needle. That makes sense, as the ionic wind is mainly due to the high EHD force in the close vicinity of the needle tip and not to the force and the motion of ions in the drift zone. Secondly, the angled tip, *i.e.,* the bevel of the tip, has an important effect on the ionic wind velocity.

Then, we discussed the ionic wind dynamics, that is to say, the behavior of the ionic wind as a function of time. We have seen that when the high voltage is suddenly switched on, a thin ionic wind jet starts to flow from the needle tip and progresses toward the plate with a velocity

of a few m/s. When the ionic wind jet impacts the plate, two counter-vortices are formed on both sides of the impact point. These two vortices in 2D correspond in reality to a single 3D vortex with a ring shape.

We have presented the results of two research teams that experimentally studied the role of Trichel pulses and breakdown streamers in the dynamics of the ionic wind. First, we highlighted that the negative ionic wind jet was relatively wide, stable, and slow. Moreover, we have observed that the presence of Trichel pulses resulted in the formation of small mushroom-like jets with very surprising properties. However, the EHD phenomena taking place at the front of these jets have not been precisely identified, and much work remains to be done to understand what happens during the formation of these unsteady jets. Secondly, in the case of a positive corona discharge, we have shown that the jet is faster, thinner, more pointed, and very unstable, rather like a pulsed jet. The frequency analysis of the ionic wind velocity highlighted that the latter was pulsed at the same frequency as the breakdown streamers, showing without any doubt the key role of streamers in the ionic wind dynamics. However, the physical explanation for the role of streamers is not known at all. It is not known whether the fact that the velocity is pulsed indicates that each streamer is the source of a strong EHD force as it propagates from the tip to the plate or whether it is that each streamer leaves an important space charge after its propagation. That said, it does seem that the duration of breakdown streamers (around 100 ns) is too small to significantly modify the whole ionic wind, as the time between two streamers is around a few hundred microseconds. Consequently, we can legitimately think that the increase in velocity occurs just after the streamer propagation due to a strong remaining positive space charge.

Furthermore, regarding the temporal behavior of the ionic wind, we saw that its velocity versus time could be controlled by adjusting the waveform of the applied high voltage.

Finally, in the last part of the present article, we tried to explain the experimental results presented in the previous parts with the help of numerical simulations. In general, these numerical simulations are very useful as they can allow us to explain experimental observations, and better understand the physical phenomena at the origin of the ionic wind. In practice, they help explain the time-averaged behavior of corona discharges and the ionic wind they produce. For instance, they helped us to understand why the jet induced by a negative corona discharge is usually slower and wider than the one induced by a positive corona discharge. Moreover, they allow us to bring to light the role of the breakdown streamers.

It is very complicated to simulate the temporal behavior of ionic wind for several reasons. First, since the ionic wind originates in the ionization zone, the mesh size must be very fine (a few µm around the tip). Secondly, the time scales of plasma physics and fluid mechanics are very different. A Trichel and streamer pulse having a width of a few hundred nanoseconds, the time step must be much smaller than that. Finally, to run simulations faithful to reality, we should consider many chemical reactions inside the discharge, making these numerical simulations very time-consuming.

Unfortunately, we are not close to being able to describe all the physics behind the ionic wind. Our computational capabilities are still too weak to carry out complete simulations of the phenomenon, and we cannot measure the density of positive and negative ions between the two electrodes with great spatial and temporal precision.

This clearly shows that there is still a lot of experimental and numerical simulation work to be done to understand the ionic wind better and optimize all the electric and geometric

input parameters according to the targeted application. Finally, since the applications of ionic wind will most likely be at small scales, ranging from a few millimeters to the sub-millimeter scale, it will also be necessary to study the behavior of corona discharges and the ionic wind they can generate at these scales.

Acknowledgments

This work pertains to the French government program France 2030 (LABEX INTERACTIFS, reference ANR-11-LABX-0017-01 and EUR INTREE, reference ANR-18-EURE-0010).

References

1. Warburg, E. Ueber die Spitzenentladung. *Ann. Phys. Chem.* **303**, 69–83 (1899).
2. Chattock, A. P. XLIV. *On the velocity and mass of the ions in the electric wind in air*. *Philos. Mag. Ser. 5* **48**, 401–420 (1899).
3. Zeleny, J. The Discharge of Electricity from Pointed Conductors. *Phys. Rev. Ser. I* **26**, 129–154 (1907).
4. Townsend, J. S. & Edmunds, P. J. LXXXIX. *The discharge of electricity from cylinders and points*. *Philos. Mag. Ser. 6* **27**, 789–801 (1914).
5. Kip, A. F. Positive-Point-to-Plane Discharge in Air at Atmospheric Pressure. *Phys. Rev.* **54**, 139–146 (1938).
6. Kip, A. F. Onset Studies of Positive Point-to-Plane Corona in Air at Atmospheric Pressure. *Phys. Rev.* **55**, 549–556 (1939).
7. Trichel, G. W. The Mechanism of the Negative Point to Plane Corona Near Onset. *Phys. Rev.* **54**, 1078–1084 (1938).
8. Trichel, G. W. The Mechanism of the Positive Point-to-Plane Corona in Air at Atmospheric Pressure. *Phys. Rev.* **55**, 382–390 (1939).

9. Loeb, L. B. Recent Developments in Analysis of the Mechanisms of Positive and Negative Coronas in Air. *J. Appl. Phys.* **19**, 882–897 (1948).
10. English, W. N. Positive and Negative Point-to-Plane Corona in Air. *Phys. Rev.* **74**, 170–178 (1948).
11. Gaunt, H. M. & Craggs, J. D. Electrical and Optical Characteristics of D.C. Corona Discharge. *Nature* **167**, 647–648 (1951).
12. Murphy, B. Positive-Point D.C. Corona. *Nature* **176**, 397–398 (1955).
13. Hermstein, W. Die Stromfaden-Entladung und ihr Übergang in das Glimmen. *Arch. Für Elektrotechnik* **45**, 209–224 (1960).
14. Hudson, G. G. & Loeb, L. B. Streamer Mechanism and Main Stroke in the Filamentary Spark Breakdown in Air as Revealed by Photomultipliers and Fast Oscilloscopic Techniques. *Phys. Rev.* **123**, 29–43 (1961).
15. Loeb, L. B. *Electrical Coronas, Their Basic Physical Mechanisms*. (1965).
16. Giao, T. & Jordan, J. Modes of Corona Discharges in Air. *IEEE Trans. Power Appar. Syst.* **PAS-87**, 1207–1215 (1968).
17. Sigmond, R. S. The residual streamer channel: Return strokes and secondary streamers. *J. Appl. Phys.* **56**, 1355–1370 (1984).
18. Goldman, M., Goldman, A. & Sigmond, R. S. The corona discharge, its properties and specific uses. *Pure Appl. Chem.* **57**, (1985).
19. Chang, J.-S., Lawless, P. A. & Yamamoto, T. Corona discharge processes. *IEEE Trans. Plasma Sci.* **19**, 1152–1166 (1991).
20. Cabeo, N. Philosophia Magnetica. (1629).
21. Harney, D. J. An aerodynamic study of electric wind. (1957).
22. Robinson, M. Movement of air in the electric wind of the corona discharge. *Trans. Am. Inst. Electr. Eng. Part Commun. Electron.* **80**, 143–150 (1961).
23. Robinson, M. A History of the Electric Wind. *Am. J. Phys.* **30**, 366–372 (1962).
24. Stuetzer, O. M. Ion Drag Pressure Generation. 984–994 (1959).

25. Christenson, E. A. & Moller, P. S. Ion-neutral propulsion in atmospheric media. *AIAA J.* **5**, 1768–1773 (1967).
26. Tsubone, H. *et al.* Flow characteristics of dc wire-non-parallel plate electrohydrodynamic gas pumps. *J. Electrost.* **66**, 115–121 (2008).
27. Kim, C., Park, D., Noh, K. C. & Hwang, J. Velocity and energy conversion efficiency characteristics of ionic wind generator in a multistage configuration. *J. Electrost.* **68**, 36–41 (2010).
28. Lee, S. J., Li, L., Kwon, K., Kim, W. & Kim, D. Parallel integration of ionic wind generators on PCBs for enhancing flow rate. *Microsyst. Technol.* **21**, 1465–1471 (2015).
29. Jaworek, A., Marchewicz, A., Sobczyk, A. T., Krupa, A. & Czech, T. Two-stage electrostatic precipitators for the reduction of PM2.5 particle emission. *Prog. Energy Combust. Sci.* **67**, 206–233 (2018).
30. Wang, Y. *et al.* Insights into the role of ionic wind in honeycomb electrostatic precipitators. *J. Aerosol Sci.* **133**, 83–95 (2019).
31. Jaworek, A., Marchewicz, A., Sobczyk, A. T., Krupa, A. & Czech, T. Recent advances in electrostatic precipitation of particles from flue gases generated by domestic heating appliances. A brief outlook. *J. Electrost.* **129**, 103922 (2024).
32. Wang, J., Zhu, T., Cai, Y., Zhang, J. & Wang, J. Review on the recent development of corona wind and its application in heat transfer enhancement. *Int. J. Heat Mass Transf.* **152**, 119545 (2020).
33. Anukiruthika, T., Moses, J. A. & Anandharamakrishnan, C. Electrohydrodynamic drying of foods: Principle, applications, and prospects. *J. Food Eng.* **295**, 110449 (2021).
34. Moreau, E. Airflow control by non-thermal plasma actuators. *J. Phys. Appl. Phys.* **40**, 605–636 (2007).
35. Benard, N. & Moreau, E. Electrical and mechanical characteristics of surface AC dielectric barrier discharge plasma actuators applied to airflow control. *Exp. Fluids* **55**, (2014).
36. Kotsonis, M. Diagnostics for characterisation of plasma actuators. *Meas. Sci. Technol.* **26**, 092001 (2015).

37. Xu, H. *et al.* Flight of an aeroplane with solid-state propulsion. *Nature* **563**, 532–535 (2018).
38. Grosse, S., Moreau, E. & Binder, N. Modeling of the Flight Performance of a Plasma-Propelled Drone: Limitations and Prospects. *Drones* **8**, 114 (2024).
39. Hari Prasad, H. K. *et al.* A laser-microfabricated electrohydrodynamic thruster for centimeter-scale aerial robots. *PLOS ONE* **15**, e0231362 (2020).
40. Nelson, C. L. & Drew, D. S. High Aspect Ratio Multi-Stage Ducted Electroaerodynamic Thrusters for Micro Air Vehicle Propulsion. *IEEE Robot. Autom. Lett.* **9**, 2702–2709 (2024).
41. Fridlender, T., Benard, N., Bonnet, J. P. & Moreau, E. Mixing Enhancement Downstream of an Active Square-Mesh Grid Using Plasma Actuation. *AIAA J.* 1–5 (2024) doi:10.2514/1.J063712.
42. Johnson, M. J. & Go, D. B. Recent advances in electrohydrodynamic pumps operated by ionic winds: a review. *Plasma Sources Sci. Technol.* **26**, 103002 (2017).
43. Qu, J. *et al.* A review on recent advances and challenges of ionic wind produced by corona discharges with practical applications. *J. Phys. Appl. Phys.* **55**, 153002 (2022).
44. Hauksbee, F. Physico-mechanical experiments on various subjects. (1709).
45. Newton, I. Optics. (1718).
46. Nollet, J. A. *Leçons de Physique Expérimentale*. (1743).
47. Cavallo, T. *A Complete Treatise of Electricity in Theory and Practice: With Original Experiments*. (1777).
48. Faraday, M. *Experimental Researches in Electricity*. (1839).
49. Maxwell, J. *A Treatise on Electricity and Magnetism*. (Oxford Clarendon, 1873).
50. Mascart, M. E. *Traité d'électricité Statique*. (1876).
51. Moreau, E., Audier, P., Orriere, T. & Benard, N. Electrohydrodynamic gas flow in a positive corona discharge. *J. Appl. Phys.* **125**, 133303 (2019).
52. Chen, S., Zhu, Y., Tu, J. & Wang, F. Numerical investigation of an electroaerodynamic driven aeroplane: electrical properties, ionic wind and flight performance. *J. Phys. Appl. Phys.* **52**, 365203 (2019).

53. Mantach, S. & Adamiak, K. A double-vortex EHD flow pattern generated by negative corona discharge in point-plane geometry. *J. Electrost.* **93**, 118–124 (2018).
54. Mizeraczyk, J., Berendt, A., Podliński, J. & Niewulis, A. Evolution of Electrohydrodynamic Flow of Suspended Particles in a Needle-to-Plate Negative DC Corona Discharge in Air. Preprint at https://doi.org/10.34343/ijpest.2016.10.01.057 (2016).
55. Advances in electroaerodynamic thrusters for & Gomez Vega N. Advances in electroaerodynamic thrusters for aircraft propulsion. (2023).
56. Lai, F. C. EHD gas pumping – A concise review of recent development. *J. Electrost.* **106**, 103469 (2020).
57. Rezaeiha, A. & Kotsonis, M. Plasma Actuation for Mitigation of Fluctuating Loads on Airfoils: An Experimental Study. *J. Phys. Conf. Ser.* **1618**, 052067 (2020).
58. Wang, J.-J., Choi, K.-S., Feng, L.-H., Jukes, T. N. & Whalley, R. D. Recent developments in DBD plasma flow control. *Prog. Aerosp. Sci.* **62**, 52–78 (2013).
59. Benard, N., Mizuno, A. & Moreau, E. Manipulation of a grid-generated mixing with an active honeycomb dielectric barrier plasma discharge. *Appl. Phys. Lett.* **107**, 233508 (2015).
60. Moreau, E., Benard, N., Lan-Sun-Luk, J.-D. & Chabriat, J.-P. Electrohydrodynamic force produced by a wire-to-cylinder dc corona discharge in air at atmospheric pressure. *J. Phys. Appl. Phys.* **46**, 475204 (2013).
61. Defoort, E., Bellanger, R., Batiot-Dupeyrat, C. & Moreau, E. Ionic wind produced by a DC needle-to-plate corona discharge with a gap of 15 mm. *J. Phys. Appl. Phys.* **53**, 175202 (2020).
62. Ferreira, G. F. L., Oliveira, O. N. & Giacometti, J. A. Point-to-plane corona: Current-voltage characteristics for positive and negative polarity with evidence of an electronic component. *J. Appl. Phys.* **59**, 3045–3049 (1986).
63. Meng, X., Zhang, H. & Zhu, J. (Jesse). A general empirical formula of current–voltage characteristics for point-to-plane geometry corona discharges. *J. Phys. Appl. Phys.* **41**, 065209 (2008).

64. Goossens, O. *et al.* The DC glow discharge at atmospheric pressure. *IEEE Trans. Plasma Sci.* **30**, 176–177 (2002).

65. Zhang, Y., Liu, L., Chen, Y. & Ouyang, J. Characteristics of ionic wind in needle-to-ring corona discharge. *J. Electrost.* **74**, 15–20 (2015).

66. Yan, H., Benard, N. & Moreau, E. On the different regimes of positive DC corona discharges as a function of electrical and geometrical parameters. *J. Appl. Phys.* **133**, 013301 (2023).

67. Moreau, E., Audier, P. & Benard, N. Ionic wind produced by positive and negative corona discharges in air. *J. Electrost.* **93**, 85–96 (2018).

68. Chen, S., van den Berg, R. G. W. & Nijdam, S. The effect of DC voltage polarity on ionic wind in ambient air for cooling purposes. *Plasma Sources Sci. Technol.* **27**, 055021 (2018).

69. Hermstein, W. Die Stromfaden-Entladung und ihr Übergang in das Glimmen. *Arch. Für Elektrotechnik* **45**, 209–224 (1960).

70. Marode, E. The mechanism of spark breakdown in air at atmospheric pressure between a positive point and a plane. I. Experimental: Nature of the streamer track. *J. Appl. Phys.* **46**, 2005–2015 (1975).

71. Eichwald, O. *et al.* Experimental analysis and modelling of positive streamer in air: towards an estimation of O and N radical production. *J. Phys. Appl. Phys.* **41**, 234002 (2008).

72. Li, Z., Zhang, B., He, J. & Xu, Y. Influence of gap spacing on the characteristics of Trichel pulse generated in point-to-plane discharge gaps. *Phys. Plasmas* **21**, 012113 (2014).

73. Dordizadeh, P., Adamiak, K. & Castle, G. S. P. Experimental study of the characteristics of Trichel pulses in the needle-plane negative corona discharge in atmospheric air. *J. Electrost.* **88**, 49–54 (2017).

74. Berard, P., Lacoste, D. A. & Laux, C. O. Corona Discharges in Atmospheric Air Between a Wire and Two Plates. *IEEE Trans. Plasma Sci.* **39**, 2248–2249 (2011).

75. Moreau, E. & Defoort, E. Ionic wind of a needle-to-plate dielectric barrier discharge. *J. Electrost.* **120**, 103768 (2022).

76. Moreau, E. & Defoort, E. Effect of the high voltage waveform on the ionic wind produced by a needle-to-plate dielectric barrier discharge. *Sci. Rep.* **12**, 18699 (2022).
77. Sánchez, M. & Conesa, A. J. On the prediction of current-voltage characteristics for positive wire-to-cylinder corona discharge. *J. Electrost.* **96**, 23–29 (2018).
78. Xu, P., Zhang, B., Chen, S. & He, J. Influence of humidity on the characteristics of positive corona discharge in air. *Phys. Plasmas* **23**, 063511 (2016).
79. Nouri, H., Zouzou, N., Moreau, E., Dascalescu, L. & Zebboudj, Y. Effect of relative humidity on current–voltage characteristics of an electrostatic precipitator. *J. Electrost.* **70**, 20–24 (2012).
80. Grosse, S., Benard, N. & Moreau, E. Current, thrust, and power of a corona discharge plasma thruster at tropospheric altitude. *J. Phys. Appl. Phys.* **58**, 095201 (2025).
81. Zhang, Y., Xia, Q., Jiang, Z. & Ouyang, J. Trichel pulse in various gases and the key factor for its formation. *Sci. Rep.* **7**, 10135 (2017).
82. Grosse, S., Benard, N. & Moreau, E. Electroaerodynamic thrusters: Influence of a freestream on the current, ionic wind, and force produced by a DC corona discharge. *J. Electrost.* **130**, 103950 (2024).
83. Martell, B. C., Strobel, L. R. & Guerra-Garcia, C. DC-driven positive streamer coronas in airflow. *Plasma Sources Sci. Technol.* **31**, 085014 (2022).
84. Guan, Y., Vaddi, R. S., Aliseda, A. & Novosselov, I. Experimental and numerical investigation of electrohydrodynamic flow in a point-to-ring corona discharge. *Phys. Rev. Fluids* **3**, 043701 (2018).
85. Guan, Y., Vaddi, R. S., Aliseda, A. & Novosselov, I. Analytical model of electro-hydrodynamic flow in corona discharge. *Phys. Plasmas* **25**, 083507 (2018).
86. Drews, A. M., Cademartiri, L., Whitesides, G. M. & Bishop, K. J. M. Electric winds driven by time oscillating corona discharges. *J. Appl. Phys.* **114**, 143302 (2013).
87. Moreau, E. & Touchard, G. Enhancing the mechanical efficiency of electric wind in corona discharges. *J. Electrost.* **66**, 39–44 (2008).

88. Moreau, E. & Benard, N. Ionic wind produced by volume corona discharges and surface dielectric barrier discharges: What role do streamers play? *J. Electrost.* **132**, 103988 (2024).
89. Ashikhmin, I., Stishkov, Y. K. & Yakovlev, V. Experimental study of kinematic structure of ionic wind in needle-torus electrode system in air. *Int. J. Plasma Environ. Sci. Technol.* **9**, 13–17 (2015).
90. Zhang, T., Zhang, Y., Ji, Q., Li, B. & Ouyang, J. Characteristics and underlying physics of ionic wind in dc corona discharge under different polarities*. *Chin. Phys. B* **28**, 075202 (2019).
91. Moreau, E., Souakri, S., Bellanger, R. & Benard, N. Ionic wind produced by a millimeter-gap DC corona discharge ignited between a plate and an inclined needle. Preprint at https://doi.org/10.34343/ijpest.2021.15.e01001 (2021).
92. Yang, Y. *et al.* Comparison of Initiation and Temporal Evolution of Positive and Negative Ionic Wind Under Needle-to-Plate Electrode. *IEEE Trans. Plasma Sci.* **51**, 352–358 (2023).
93. Elagin, I. A., Begal', D. I., Ashikhmin, I. A. & Stishkov, Yu. K. Change in the direction of electric wind from a wire electrode tilted relative to a grounded plane. *Tech. Phys. Lett.* **43**, 98–100 (2017).
94. Elagin, I., Samusenko, A. & Chirkov, V. Numerical study of the needle inclination angle effect on the ionic wind direction. *Int. J. Plasma Environ. Sci. Technol.* Vol. 14 (2020).
95. Rubinetti, D. *et al.* Energy-saving discharge needle shape for electrohydrodynamic airflow generation. *J. Electrost.* **127**, 103876 (2024).
96. Lee, J. R. & Lau, E. V. Convective heat transfer enhancement of ionic wind under variable air pressures. *Int. J. Therm. Sci.* **160**, 106657 (2021).
97. Zhao, Y., Chen, S., Li, K., Wang, T. & Wang, F. Influence of humidity and air pressure on thrust characteristics of ion wind propulsion systems. *J. Phys. Appl. Phys.* **57**, 415201 (2024).
98. Zeng, M. J., Qu, Z. G. & Zhang, J. F. Negative corona discharge and flow characteristics of a two-stage needle-to-ring configuration ionic wind pump for temperature and relative humidity. *Int. J. Heat Mass Transf.* **201**, 123561 (2023).

99. Giepman, R. H. M. & Kotsonis, M. On the mechanical efficiency of dielectric barrier discharge plasma actuators. *Appl. Phys. Lett.* **98**, 221504 (2011).

100. Benard, N., Debien, A. & Moreau, E. Time-dependent volume force produced by a non-thermal plasma actuator from experimental velocity field. *J. Phys. Appl. Phys.* **46**, 245201 (2013).

101. Orrière, T., Moreau, É. & Pai, D. Z. Electric wind generation by nanosecond repetitively pulsed microplasmas. *J. Phys. Appl. Phys.* **52**, 464002 (2019).

102. Park, S., Cvelbar, U., Choe, W. & Moon, S. Y. The creation of electric wind due to the electrohydrodynamic force. *Nat. Commun.* **9**, 371 (2018).

103. Du, S. *et al.* Laser guided ionic wind. *Sci. Rep.* **8**, 13511 (2018).

104. Mizeraczyk, J., Berendt, A. & Podlinski, J. Temporal and spatial evolution of EHD particle flow onset in air in a needle-to-plate negative DC corona discharge. *J. Phys. Appl. Phys.* **49**, 205203 (2016).

105. Mizeraczyk, J., Berendt, A. & Akishev, Y. Controlled generation of a single Trichel pulse and a series of single Trichel pulses in air. *J. Phys. Appl. Phys.* **51**, 155204 (2018).

106. Mizeraczyk, J. & Berendt, A. Introduction to investigations of the negative corona and EHD flow in gaseous two-phase fluids. *Plasma Sci. Technol.* **20**, 054020 (2018).

107. Bouazza, M. R. *et al.* Effect of the EHD Force on the Spatial Distribution of Neutral Species Generated by a Positive and Negative Corona Discharge. in *2022 IEEE 21st International Conference on Dielectric Liquids (ICDL)* 1–4 (IEEE, Sevilla, Spain, 2022). doi:10.1109/ICDL49583.2022.9830955.

108. Asipuela, A. & Iváncsy, T. Study and Numerical Simulation of Negative and Positive Corona Discharge: A Review. *Period. Polytech. Electr. Eng. Comput. Sci.* **66**, 294–300 (2022).

109. Liu, L. & Becerra, M. An efficient model to simulate stable glow corona discharges and their transition into streamers. *J. Phys. Appl. Phys.* **50**, 105204 (2017).

110. Chen, S., Nobelen, J. C. P. Y. & Nijdam, S. A self-consistent model of ionic wind generation by negative corona discharges in air with experimental validation. *Plasma Sources Sci. Technol.* **26**, 095005 (2017).

111. Ferreira, N. G. C. *et al.* Computational and Experimental Study of Time-Averaged Characteristics of Positive and Negative DC Corona Discharges in Point-Plane Gaps in Atmospheric Air. *IEEE Trans. Plasma Sci.* **48**, 4080–4088 (2020).

112. Chen, J. & Davidson, J. H. Model of the Negative DC Corona Plasma: Comparison to the Positive DC Corona Plasma. *Plasma Chem. Plasma Process.* **23**, 83–102 (2003).

113. Liu, L. & Becerra, M. On the transition from stable positive glow corona to streamers. *J. Phys. Appl. Phys.* **49**, 225202 (2016).

114. Dordizadeh, P., Adamiak, K. & Peter Castle, G. S. Numerical investigation of the formation of Trichel pulses in a needle-plane geometry. *J. Phys. Appl. Phys.* **48**, 415203 (2015).

115. Chung, J. H., Ahn, T. S., Sohn, D. K. & Ko, H. S. Numerical study on ionic wind from pin to mesh with hole configuration under DC negative corona discharge. *J. Phys. Appl. Phys.* **58**, 105205 (2025).

116. Loiseau, J. F., Batina, J., Noël, F. & Peyrous, R. Hydrodynamical simulation of the electric wind generated by successive streamers in a point-to-plane reactor. *J. Phys. Appl. Phys.* **35**, 1020–1031 (2002).